

submitted to *The Astrophysical Journal*

Optical, UV, and X-Ray Scattering by Interstellar Dust Grains

B.T. Draine

Princeton University Observatory, Peyton Hall, Princeton, NJ 08544;
draine@astro.princeton.edu

ABSTRACT

Scattering and absorption properties at optical, ultraviolet, and X-ray wavelengths are calculated for an interstellar dust model consisting of carbonaceous grains and amorphous silicate grains. The widely-used Henyey-Greenstein phase function provides a good approximation for the scattering phase function at wavelengths between ~ 0.4 and $1\mu\text{m}$, but fails to fit the calculated phase functions at shorter wavelengths. For $\lambda < 0.24\mu\text{m}$, the Henyey-Greenstein phase function has an absolute error $> 50\%$, and should not be used for accurate modelling in the vacuum ultraviolet. Polarization as a function of scattering angle is calculated for selected wavelengths from the infrared to the vacuum ultraviolet.

The calculations employ realistic dielectric functions with structure near X-ray absorption edges, with resulting features in absorption, scattering, and extinction. Differential scattering cross sections are calculated for energies between 0.3 and 10 keV. The median scattering angle is given as a function of energy, and simple but accurate approximations are found for the X-ray scattering properties of the dust mixture, as well as for the angular distribution of the scattered X-ray halo for dust with simple density distributions. Observational estimates of the X-ray scattering optical depth are compared to model predictions. Observations of X-ray halos to test interstellar dust grain models are best carried out using extragalactic point sources.

Subject headings: dust, extinction – polarization – scattering – ultraviolet: ISM – X-rays: ISM

1. Introduction

Interstellar grains absorb and scatter electromagnetic radiation. Reflection nebulosities are conspicuous at optical and UV wavelengths when dust is brightly illuminated by a nearby star. Dust clouds which are not unusually close to a star are illuminated by the general interstellar radiation field, and the scattered light constitutes the so-called “diffuse galactic light”. Observations of reflection nebulae and the diffuse galactic light, when compared to models, provide a means of determining the scattering properties of interstellar grains, thereby testing models for interstellar dust.

Reflection is also observable at X-ray wavelengths (Overbeck 1965; Martin 1970; Hayakawa 1973) except that in this case the extreme forward-scattering results in a “halo” of scattered X-rays within $\sim 1^\circ$ of the X-ray source, and the dust producing the scattering need not be close to the X-ray source. The observed properties of these X-ray halos also provide a test of interstellar grain models.

Photoionization and photodissociation of molecules can play a dominant role in interstellar chemistry, and the chemical structure of molecular clouds is therefore directly linked to the ability of ultraviolet starlight to penetrate into these dusty regions. Knowledge of dust scattering properties in the ultraviolet is therefore required for realistic modelling of interstellar clouds.

The nature of interstellar grains remains uncertain (see Draine 2003, and references therein). This paper will examine the scattering properties predicted for a grain model consisting of two separate grain populations – carbonaceous grains and silicate grains. With the grains approximated by homogeneous spheres with the size distribution found by Weingartner & Draine (2001; hereafter WD01), this grain model is consistent with the observed interstellar extinction law, and the same grain model can reproduce the observed infrared emission from interstellar dust (Li & Draine 2001, 2002), and is consistent with the X-ray scattering halo observed around Nova Cygni 1992 (Draine & Tan 2003). The carbonaceous grains are assumed to be primarily carbon when the grains are large, but to extend down to very small sizes with the smallest grains being individual polycyclic aromatic hydrocarbon molecules. The scattering is dominated by grains with radii $a \gtrsim 100 \text{ \AA}$, containing $\gtrsim 10^6$ atoms; carbonaceous grains in this size range are modelled using the optical properties of graphite.

The primary objective of this paper is to calculate the scattering and extinction properties of this dust model, and to make these results available for use in radiative transfer calculations and for comparison with observations. The paper has three relatively independent parts, and readers may wish to proceed directly to the material of interest to them.

The first part of this paper – §2 – is concerned with the dielectric functions of graphite and MgFeSiO_4 from infrared to X-ray energies. The resulting dielectric functions satisfy the Kramers-Kronig relations as well as the oscillator strength sum rule.

The second part – §3 – concerns the scattering properties of interstellar dust at optical and ultraviolet energies, as calculated for the carbonaceous-silicate grain model. We show the scattering phase function at selected wavelengths from the SDSS z band ($\lambda = 8930 \text{ \AA}$) to the vacuum ultraviolet ($\lambda = 1820 \text{ \AA}$). Scattering properties are calculated for average diffuse Milky Way dust with $R_V = 3.1$, and also for models for dust in the LMC and SMC. In §3.2 we show the degree of polarization as a function of scattering angle for selected wavelengths. The Henyey-Greenstein phase function is often used to approximate the anisotropic scattering properties of interstellar dust. In §3.3 we show that the Henyey-Greenstein function provides $\sim 10\%$ accuracy for modelling scattering at $\lambda \gtrsim 5000 \text{ \AA}$, but is a poor approximation in the ultraviolet. We therefore caution against use of the Henyey-Greenstein phase function in modelling the ultraviolet properties of reflection nebulae, or

in modelling penetration of ultraviolet radiation into molecular clouds.

The third part of the paper – §§4–6 – examines the X-ray scattering properties of interstellar dust, including structure near X-ray absorption edges. The angular distribution of the scattered X-rays is discussed: the median scattering angle $\theta_{s,50}$ is found as a function of energy, and a simple analytic approximation to the differential scattering cross section is presented. In §5 we provide simple approximations for the intensity distribution in X-ray scattering halos for simple dust density distributions, and in §6 we discuss observations of X-ray scattering halos, and values of total scattering cross section derived from these observations. We conclude that the observational situation is unclear at this time, due to the combined effects of instrumental limitations and uncertainties in the spatial distribution of the dust, but the silicate/carbonaceous grain model appears to be in agreement with the overall body of observational data. Future observations using extragalactic point sources could transcend the uncertainties concerning the dust spatial distribution.

The principal results are summarized in §7

2. Dielectric Function

Our objective here is to obtain continuous complex dielectric functions $\epsilon(\omega) = \epsilon_1 + i\epsilon_2$ which can be used to calculate scattering and absorption by these grains from the submm to hard X-rays. For material at LTE (i.e., no population inversions), the dielectric function must have $\epsilon_2 \geq 0$. Causality requires that the dielectric function must satisfy the Kramers-Kronig relations (Landau & Lifshitz 1960), in particular

$$\epsilon_1(\omega) = 1 + \frac{2}{\pi} P \int_0^\infty \frac{\epsilon_2(x) x dx}{x^2 - \omega^2} \quad , \quad (1)$$

where P indicates that the principal value is to be taken. We will proceed by first specifying $\epsilon_2(\omega)$ at all frequencies, and then obtaining $\epsilon_1(\omega)$ using eq. (1).

In addition to satisfying the Kramers-Kronig relations, the dielectric function must obey the sum rule (Altarelli et al. 1972)

$$\int_0^\infty \omega \epsilon_2(\omega) d\omega = \frac{2\pi^2 e^2}{m_e} \sum_j n_j Z_j \quad , \quad (2)$$

where n_j is the number density and Z_j is the number of electrons in element j . Thus we may define the effective number of electrons per molecule

$$n_{\text{eff}}(\omega) \equiv \frac{m_e V_0}{2\pi^2 e^2} \int_0^\omega x \epsilon_2(x) dx \quad , \quad (3)$$

where V_0 is the volume per molecule, and $n_{\text{eff}}(\infty) =$ the total number of electrons per molecule.

Ideally, $\epsilon_2(\omega)$ would be measured in the laboratory for the materials of interest. At energies below $\sim 20\text{--}30$ eV the optical constants can be characterized using transmission and ellipsometric

studies, but calibrated experimental measurements are usually unavailable at X-ray energies. At high energies $\hbar\omega \gtrsim 100$ eV, $\epsilon_2(\omega)$ for a material can be approximated by summing the atomic absorption cross sections of the constituent atoms:

$$\epsilon_2(\omega) \approx \frac{c}{\omega} \sum_j n_j \sum_s \sigma_{j,s}(\omega) \quad , \quad (4)$$

where $\sigma_{j,s}$ is the atomic absorption cross section contributed by electronic shell s of element j . Eq. (4) assumes that $|\epsilon - 1| \ll 1$, which is valid at X-ray energies.

At energies well above the photoionization threshold for shell s , atomic photoionization is to high momentum free electron states which will have counterparts in the solid, and we can approximate $\sigma_{j,s}$ by the atomic photoionization cross section fitting functions $\sigma_{j,s}^{pi}(\omega)$ estimated for inner shell electrons by Verner & Yakovlev (1995), and for outer-shell electrons by Verner et al. (1996), as implemented in the Fortran routine `phfit2.f` (Verner 1996). Near threshold, however, the photoabsorption cross section $\sigma_{j,s}(\omega)$ depends on the band structure of the solid, leading to “Near Edge X-ray Absorption Fine Structure” (NEXAFS), which could in principle permit identification of interstellar grain materials through observations of X-ray absorption and scattering near absorption edges (Martin 1970; Woo 1995).

2.1. Graphite

We will assume that interstellar grains are constructed primarily from two distinct substances: carbonaceous material and amorphous silicate material. In ultrasmall grains, containing less than $\sim 10^5$ atoms, the carbonaceous material has the properties of polycyclic aromatic hydrocarbon molecules. Because of their small size, scattering by these grains is negligible, and the absorption and emission from these grains can be calculated using absorption cross sections estimated for PAH molecules or ions (Draine & Li 2001; Li & Draine 2001).

In the larger carbonaceous grains, the nature of the carbon material is less certain. The carbon atoms could be arranged in a graphitic structure (pure sp^2 bonding) or there might be a mixture of sp^2 (graphitic) and sp^3 (diamond-like) bonding, perhaps also with some aliphatic (chainlike) hydrocarbon material as well. We will assume that the optical response of the carbonaceous material in the grains containing $\gtrsim 10^5$ atoms can be approximated by graphite, with density $\rho = 2.2$ g cm $^{-3}$.

Graphite is anisotropic, with the crystal “c axis” normal to the basal plane. In a cartesian coordinate system with $\hat{\mathbf{z}} \parallel c$, the dielectric tensor is diagonal with eigenvalues $(\epsilon_{\perp}, \epsilon_{\perp}, \epsilon_{\parallel})$.

The dielectric functions ϵ_{\perp} and ϵ_{\parallel} were estimated by Draine & Lee (1984, hereafter DL84) and Laor & Draine (1993). For $E < 22$ eV we continue to use $\epsilon_{\parallel,2}$ from DL84, while for $E > 22$ eV we use eq. (4) to estimate $\epsilon_{\parallel,2}$. For $E < 35$ eV we use $\epsilon_{\perp,2}$ estimated by DL84, while for $E > 35$ eV we use eq. (4) to estimate $\epsilon_{\perp,2}$. Our final $\epsilon_{\perp,2}$ and $\epsilon_{\parallel,2}$ are shown in Figures 1 and 3.

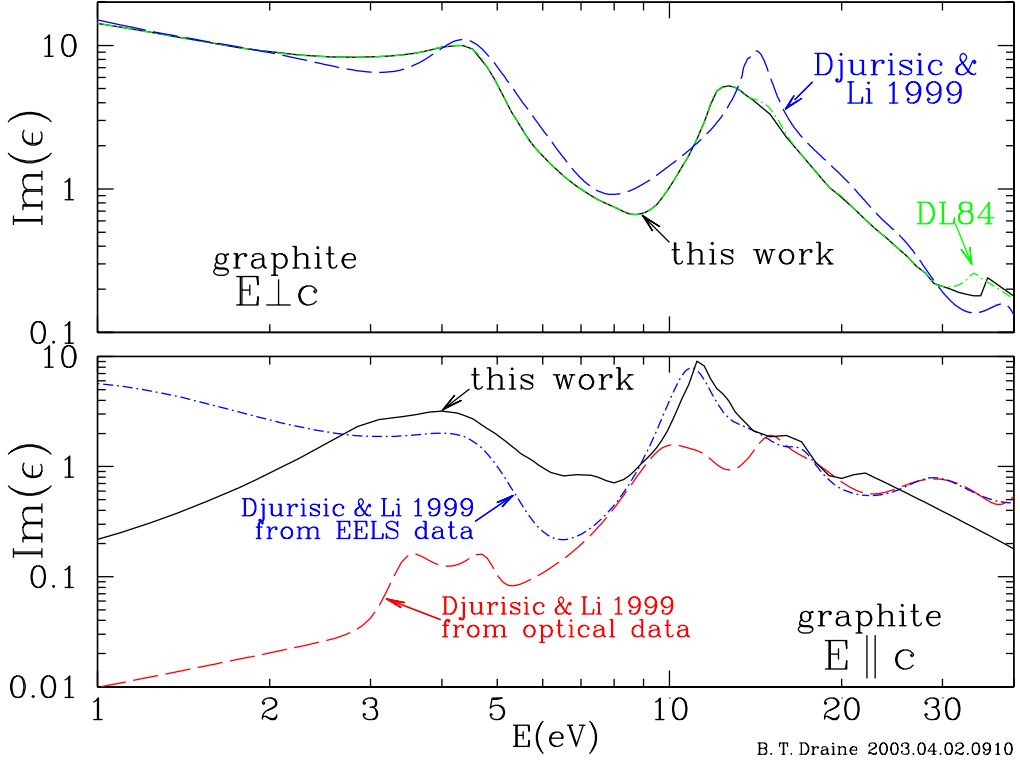


Fig. 1.— $\text{Im}(\epsilon)$ for graphite at $E < 40$ eV (see text). The ϵ_{\perp} adopted here is equal to ϵ_{\perp} adopted by DL84 below 30 eV. Also shown, for comparison, are estimates for ϵ_{\perp} and ϵ_{\parallel} by Djuricic & Li (1999).

Djuricic & Li (1999) recently reestimated ϵ_{\perp} and ϵ_{\parallel} for $\hbar\omega < 40$ eV by fitting a model to the available experimental evidence. Their estimate for $\text{Im}(\epsilon_{\perp})$ is shown in Figure 1. We see that it is generally similar to the DL84 dielectric function, although with a pronounced peak at ~ 14 eV in place of the broader feature peaking at ~ 12 eV in the DL84 estimate of ϵ_{\perp} .

For $E \parallel c$, however, Djuricic & Li concluded that optical ellipsometric measurements are inconsistent with the dielectric function estimated from electron energy loss spectroscopy (EELS). Djuricic & Li obtained $\epsilon_{\parallel}(\omega)$ from the optical measurements and then independently from the EELS data. These two estimates for ϵ_{\parallel} – which differ substantially – are shown in Figure 1. The Djuricic & Li estimate based on EELS data is fairly similar to the DL84 estimate for ϵ_{\parallel} (which was based in part on experimental papers using EELS). Given the inconsistencies among the different experimental investigations, ϵ_{\parallel} in the optical and UV should be regarded as uncertain.

For carbon, the only X-ray feature is the carbon K edge. We use the measured K edge X-ray absorption profile for graphite from Shimada et al. (2000) for 282 - 310 eV. Shimada et al. did not determine the absolute absorption strength. We fix the amplitude such that the oscillator strength between 282 and 320 eV is 0.38, and we smoothly connect to join the Verner & Yakovlev (1995)

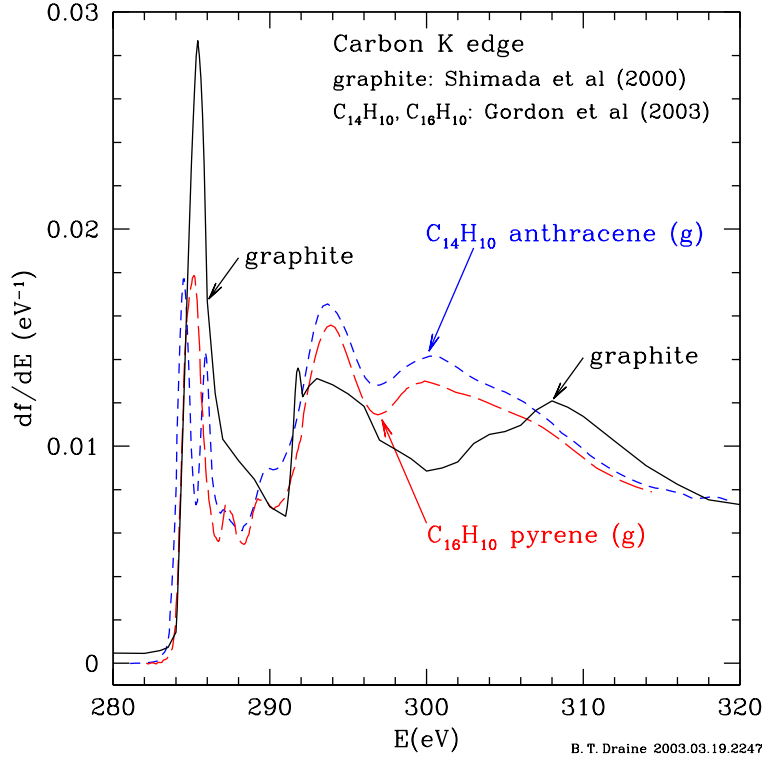


Fig. 2.— Oscillator strength for absorption near the carbon K edge in gaseous anthracene and pyrene (Gordon et al. 2003), and for graphite (Shimada et al. 2000, with normalization discussed in text).

photoionization cross section at 320 eV. In Figure 2 we show the oscillator strength density

$$\frac{df}{dE} = \frac{m_e V_0}{2\pi^2 e^2 h} \omega \epsilon_2(\omega) \quad (5)$$

near the carbon K edge for graphite, and, for comparison, for gas phase anthracene and pyrene (Gordon et al. 2003).

In Figure 3 we show $\epsilon_{\parallel,2}$ and $\epsilon_{\perp,2}$ from the optical to the X-ray region. Figure 3 shows $\epsilon_{\parallel,1}$ and $\epsilon_{\perp,1}$ obtained using eq. (1).

A useful check on the validity of the dielectric function is provided by eq. (3). Figure 4 shows that $n_{\text{eff}}(\omega) \approx 4$ just below the onset of K shell absorption, and $n_{\text{eff}}(\omega \rightarrow \infty) \rightarrow 6$, as expected for carbon.

2.2. Silicate

We will assume that the silicate material has an olivine composition, $\text{Mg}_{2x}\text{Fe}_{2(1-x)}\text{SiO}_4$. Mg and Fe are approximately equally abundant in the ISM, and both reside primarily in interstellar grains. It is therefore reasonable to take the silicate grain composition to be MgFeSiO_4 , although

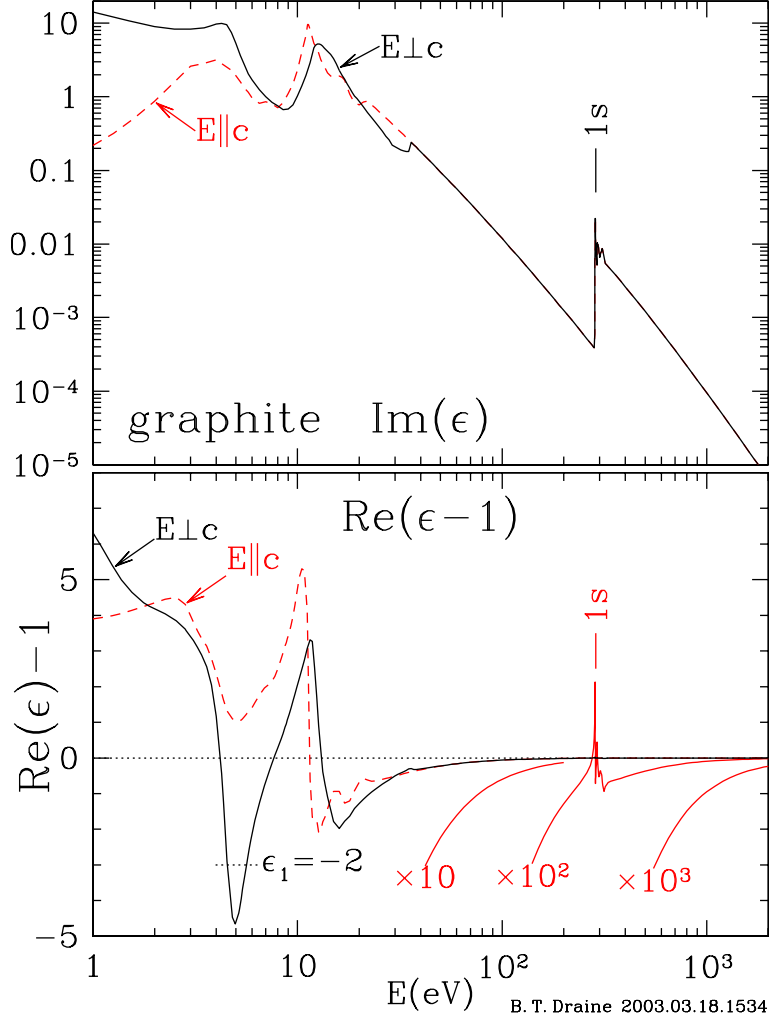


Fig. 3.— $\text{Im}(\epsilon)$ and $\text{Re}(\epsilon - 1)$ for graphite from 1 eV to 2 keV.

it is possible that, for example, some of the Fe may be another chemical form. MgFeSiO_4 olivine has a density 3.8 g cm^{-3} , intermediate between the densities of forsterite (Mg_2SiO_4 , 3.27 g cm^{-3}) and fayalite (Fe_2SiO_4 , 4.39 g cm^{-3}), with a molecular volume $V_0 = 7.5 \times 10^{-23} \text{ cm}^3$.

For $h\nu < 18 \text{ eV}$ we will adopt ϵ_2 previously obtained by Draine & Lee (1984) for “astronomical silicate”, but with the following modifications to ϵ_2 :

1. the crystalline olivine feature at $\lambda^{-1} = 6.5 \mu\text{m}^{-1}$ – not seen in interstellar extinction or polarization (Kim & Martin 1995) – has been excised with the oscillator strength redistributed over frequencies between 8 and $10 \mu\text{m}^{-1}$ (Weingartner & Draine 2001)
2. at $\lambda > 250 \mu\text{m}$, $\epsilon_2(\omega)$ has been modified slightly, as described by Li & Draine (2001). For $250 < \lambda < 1100 \mu\text{m}$ the revised ϵ_2 is within $\pm 12\%$ of ϵ_2 adopted by DL84.

Above 30 eV, we use eq. (4) to estimate ϵ_2 from atomic photoabsorption cross sections, except near absorption edges (see below). Between 18 and 30 eV, ϵ_2 is chosen to provide a smooth join between ϵ_2 from DL84 and ϵ_2 estimated from the atomic photoabsorption cross sections.

The threshold energy for photoionization from the K shell of atomic oxygen is 544.0 eV for ionization to O II $1s2s^22p^4(^4P)$, and 548.9 eV for ionization to O II $1s2s^22p^4(^2P)$; the strong $1s-2p$ absorption line, with FWHM ≈ 0.14 eV, lies at 527.0 eV (Stolte et al. 1997). From the theoretical line profile of McLaughlin & Kirby (1998), the $1s-2p$ transition has an oscillator strength $f \approx 0.10$.

X-ray spectroscopy of several galactic X-ray sources using the *Chandra X-Ray Observatory* has detected a strong and narrow absorption line at 527.5 eV which must be the O I $1s-2p$ transition, and a nearby absorption feature at 530.8 eV, with FWHM ~ 1.0 eV (Paerels et al. 2001; Schulz et al. 2002; Takei et al. 2002). Paerels et al. and Schulz et al. suggest that the 530.8 eV feature is due to iron oxides, possibly Fe_2O_3 . However, O II is expected to have $1s-2p$ absorption at approximately this energy, and the interstellar O II abundance is probably large enough that the resulting absorption feature should be conspicuous. It therefore seems likely that the observed narrow feature at 530.8 eV is (at least primarily) O II $1s-2p$.

In the absence of published X-ray absorption spectra for amorphous silicates, we estimate the oxygen K edge absorption using measurements on crystalline olivines. Li et al. (1995) have measured Mg K edge and Si K edge absorption for forsterite Mg_2SiO_4 , and Henderson et al. (1995) have measured Fe K edge absorption in fayalite Fe_2SiO_4 . We adopt these profiles for the corresponding K edges in amorphous olivine $MgFeSiO_4$, with the absorption profile strengths adjusted to match the Verner et al. photoionization cross sections for the corresponding atoms well above threshold.

Fe L_{2,3} edge spectra for a number of minerals have been studied recently by van Aken & Liebscher (2002). The L₂ edge corresponds to the remaining $2p^5$ electrons in a $^2P_{3/2}$ term, and the L₃ edge when they are in a $^2P_{1/2}$ term. The Fe in olivine is 100% Fe^{2+} . The spin-orbit splitting for Fe^{2+} produces a 12.8 eV separation between the L₂ and L₃ maxima (van Aken & Liebscher 2002), with the L₂ peak at 721.3 eV and the L₃ peak at 708.1 eV. Following van Aken & Liebscher, we model the near-edge absorption in olivine by

$$\begin{aligned} \sigma_{L_{2,3}} = & \sigma_0 \left\{ \frac{2}{3\pi} \left[\arctan \left(\frac{\pi}{w_a} (E - E_a) \right) + \frac{\pi}{2} \right] + \frac{1}{3\pi} \left[\arctan \left(\frac{\pi}{w_b} (E - E_b) \right) + \frac{\pi}{2} \right] \right. \\ & \left. + \sum_{i=1}^4 A_i \exp \left[- \left(\frac{E - E_j}{w_j} \right)^2 \right] \right\} \end{aligned} \quad (6)$$

with $E_a = 708.65$ eV, $E_b = 721.65$ eV, and $w_a = w_b = 1$ eV. The gaussian components are located at $E_1 = 707.8$ eV, $E_2 = 710.5$ eV, $E_3 = 720.6$ eV, and $E_4 = 723.3$ eV. van Aken & Liebscher do not give values for the widths of the gaussians, but inspection of their Fig. 1 suggests $w_1 = w_2 = w_3 = w_4 = 1.25$ eV. Minerals with 100% Fe^{2+} have $A_1/A_2 \approx A_3/A_4 \approx 5$, and $A_3/A_1 \approx 0.28$. For 100% ferrous Fe we estimate $A_1 \approx 6$ from the spectrum of ilmenite $FeTiO_3$ in van Aken, Liebscher & Styrs (1998). To determine the normalization σ_0 , we require that eq. (6) match the Verner et al. cross section at 800 eV.

For some absorption edges no measurements are available for appropriate minerals. Since the near-edge absorption is proportional to the density of electronic states above the Fermi surface, the near edge spectra for different elements in a compound show considerable similarity in the dependence on energy, but with displacements in energy due to the different binding energies of the electron being excited. We use the Si K edge in forsterite Mg_2SiO_4 (Li et al. 1995), shifted in energy by $\Delta E = -1308$ eV [the difference in K edge ionization thresholds for Si I (1846 eV) and O I (538 eV)] to determine the O K edge absorption profile up to 575 eV. This results in onset of O 1s absorption at ~ 527.8 eV, and an O 1s absorption peak at 537.6 eV. The absolute absorption coefficient is fixed by requiring that the absorption at 575 eV match that calculated from the atomic photoionization cross sections.¹

A similar approach is taken for the other absorption edges, using measured profiles for Mg K edge and Si K edge absorption in forsterite Mg_2SiO_4 (Li et al. 1995), and Fe K edge absorption in fayalite Fe_2SiO_4 (Henderson et al. 1995) (see Table 1).

Although this procedure is not expected to provide accurate estimates of the near-edge absorption spectra for amorphous silicates, the provisional near-edge absorption profiles so obtained will provide a realistic example of the kind of near-edge absorption and scattering expected from interstellar grains.

Figure 5 shows $Re(\epsilon)$ obtained from $Im(\epsilon)$ using eq. (1). Figure 4 provides a check on the adopted dielectric function: $\lim_{\omega \rightarrow \infty} n_{\text{eff}} = 84.01$, in agreement with the value of 84 expected theoretically for $MgFeSiO_4$.

3. IR-Optical-UV Scattering by Interstellar Dust

3.1. Angular Distribution of Scattered Light

Weingartner & Draine (2001; hereafter WD01) obtained size distributions of spherical carbonaceous and silicate grains which reproduce the observed extinction curve both in the local Milky Way and in the Large and Small Magellanic Clouds. Here we calculate the scattering properties of these dust mixtures.

The scattering properties of a particular dust mixture X are characterized by the differential

¹Absorption near the O K edge in SiO_2 has been measured by Marcelli et al. (1985), who find an absorption peak at 540 eV in both α -quartz and glassy SiO_2 . EELS studies by Wu et al. (1996) and Sharp et al. (1996) show the peak at 535 eV for quartz, while Garvie et al. (2000) use EELS to locate the quartz peak at 537.5 eV, with the absorption edge located at ~ 535 eV. The SiO_2 polymorphs α -quartz, coesite, and stishovite have their absorption peaks within ~ 1 eV of one another (Wu et al. 1996), and likewise their absorption edges agree to within ~ 1 eV.

Table 1: X-ray Edge Absorption Parameters

material	shell	E_{min}^a (eV)	E_{peak}^b (eV)	σ_{peak}^c Mb	adopted profile	ΔE^d (eV)	ref
graphite	C 1s (K)	282	285.4	3.84	graphite	0	e
olivine	O1s (K)	527.8	537.6	1.78	Mg ₂ SiO ₄ Mg K	-1308.0	f
olivine	Mg1s (K)	1300.8	1310.6	0.80	Mg ₂ SiO ₄ Mg K	0	f
olivine	Mg 2s (L_1)	83.8	93.6	2.07	Mg ₂ SiO ₄ Mg K	-1752.0	f
olivine	Mg 2p ($L_{2,3}$)	44.7	54.5	15.7	Mg ₂ SiO ₄ Mg K	-1791.1	f
olivine	Si 1s (K)	1835.8	1845.6	0.50	Mg ₂ SiO ₄ Si K	0	f
olivine	Si 2s (L_1)	145.8	155.6	1.67	Mg ₂ SiO ₄ Si K	-1690.0	f
olivine	Si 2p ($L_{2,3}$)	95.8	105.6	18.0	Mg ₂ SiO ₄ Si K	-1740.0	f
olivine	Fe 1s (K)	7105	7123	.0544	Fe ₂ SiO ₄ Fe K	0	g
olivine	Fe 2s (L_1)	838	856	0.186	Fe ₂ SiO ₄ Fe K	-6267.	g
olivine	Fe 2p(L_2)	705	720.6	2.46	Fe ²⁺ minerals Fe L ₂	0	h
olivine	Fe 2p(L_3)	705	707.8	6.30	Fe ²⁺ minerals Fe L ₃	0	h
olivine	Fe 3s (M_1)	85	103	0.338	Fe ₂ SiO ₄ Fe K	-7020	g
olivine	Fe 3p ($M_{2,3}$)	47	65	1.41	Fe ₂ SiO ₄ Fe K	-7058	g

^aEnergy at onset of absorption^bEnergy at peak absorption^cPeak absorption cross section/atom contributed by this shell.^dEnergy shift relative to adopted profile.

eShimada et al. (2000)

fLi et al. (1995)

gHenderson et al. (1995)

hvan Aken & Liebscher (2002)

scattering cross section per H nucleon

$$\left(\frac{d\sigma_{sca}(\lambda, \theta)}{d\Omega} \right)_X \equiv \sum_j \int da \left(\frac{1}{n_H} \frac{dn_j}{da} \right)_X \left(\frac{dC_{sca}}{d\Omega} \right)_{j,a,\lambda} \quad (7)$$

where $n_H^{-1}(dn_j/da)da$ is the number of grains of type j per H nucleon with radii in $(a, a + da)$, and $(dC_{sca}/d\Omega)_{j,a,\lambda}$ is the differential scattering cross section for grain type j , radius a , at wavelength λ , for scattering angle θ , for a grain illuminated by unpolarized light. The grains are assumed to be spherical, and the differential scattering cross sections are calculated using Mie theory (Bohren & Huffman 1984). For the carbonaceous grains we use the dielectric tensor of graphite with the usual 1/3-2/3 approximation, which has been shown to provide accurate results for randomly-oriented graphite spheres (Draine & Malhotra 1993).

In Figure 6 we show the differential scattering cross section per H nucleon for $R_V = 3.1$ Milky Way dust, at the central wavelengths of SDSS z (8930Å), i (7480Å), r (6165Å), g (4685Å), and u (3550Å), Cousins I (8020Å) and R (6492Å), V (5470Å), and the F250W (2696Å), F220W (2220Å),

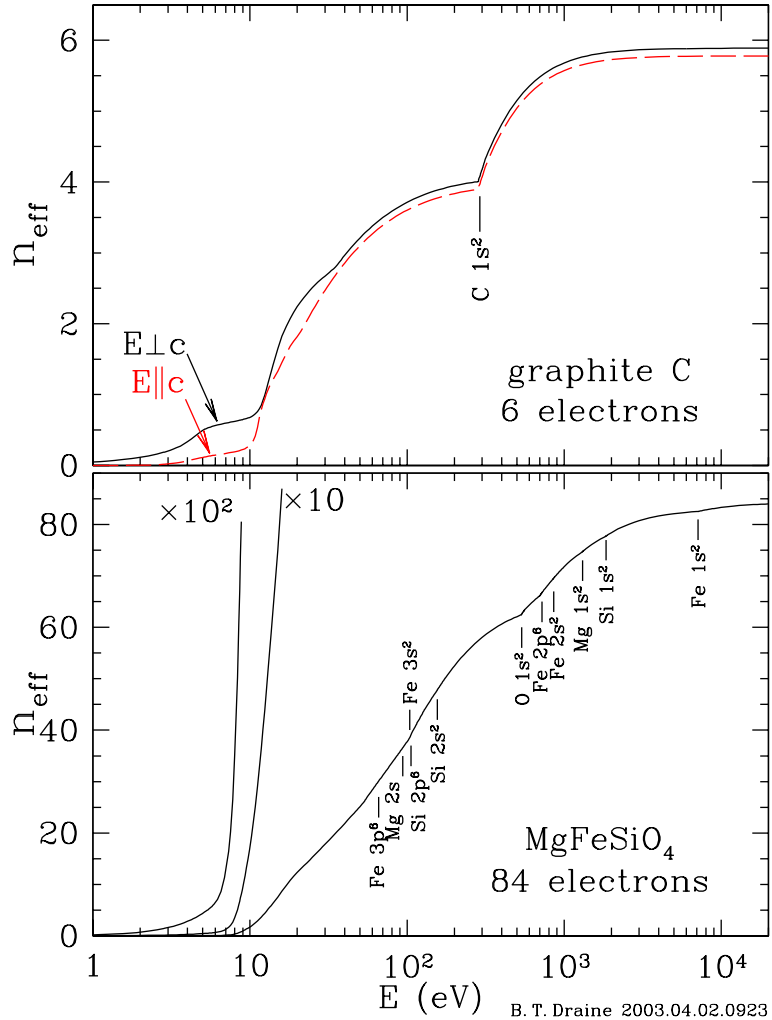


Fig. 4.— Effective number of electrons n_{eff} as a function of photon energy for graphite and MgFeSiO_4 .

and F25CN182 (1820Å) filters for the Space Telescope Imaging Spectrograph (STIS). The scattering becomes stronger and more forward-throwing at shorter wavelengths.

To see the sensitivity to variations in the dust mixture, Fig. 6 also shows $d\sigma_{\text{sca}}/d\Omega$ calculated for the WD01 dust mixtures for the “average LMC” and the SMC bar. The calculated scattering closely resembles the Milky Way scattering, but with an overall reduction of about a factor of 4 for the LMC, and a factor of 8 for the SMC, in line with the overall dust and metal abundance relative to the Milky Way.²

²Ne/H is $\sim 30\%$ of solar in the LMC and $\sim 14\%$ of solar in the SMC (Dufour 1984; Kurt & Dufour 1998). In the LMC, $E(B-V)/N_{\text{H}}$ is $\sim 40\%$ of the local Milky Way value (Koornneef 1982; Fitzpatrick 1985) while in the SMC it is only $\sim 13\%$ of the local value (Fitzpatrick 1986; Misselt et al. 1999).

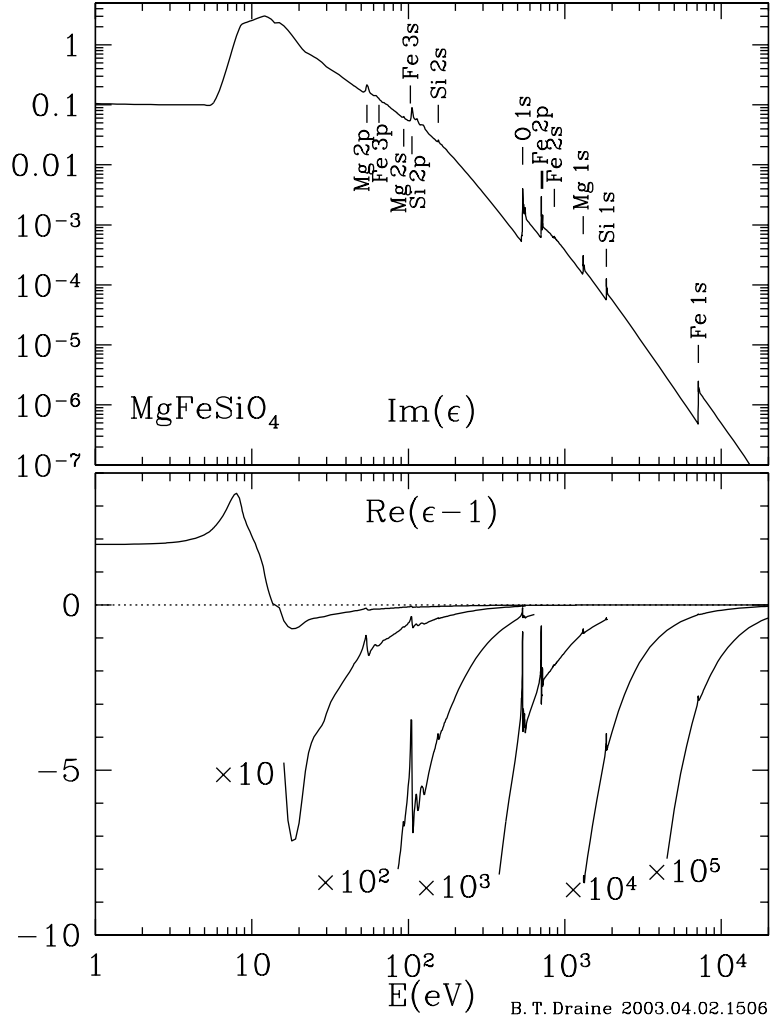


Fig. 5.— $\text{Im}(\epsilon)$ and $\text{Re}(\epsilon - 1)$ for silicate MgFeSiO_4 .

3.2. Polarization of Scattered Light

Even when a grain is illuminated by unpolarized light, the scattered radiation is generally polarized. The degree of polarization depends upon both the scattering angle and the wavelength of the radiation. The fractional polarization $P \equiv (I_{\perp} - I_{\parallel})/(I_{\perp} + I_{\parallel})$, where I_{\perp}, I_{\parallel} are the intensities of scattered light in polarization modes perpendicular or parallel to the scattering plane.

The polarization P of the scattered light is shown in Fig. 7 as a function of scattering angle θ for Milky Way dust with $R_V = 3.1$, at 11 different wavelengths. Rayleigh scattering would have $P = (1 - \cos^2 \theta)/(1 + \cos^2 \theta)$, with $P = 1$ for $\theta = 90^\circ$. At long wavelengths, the polarization has a distinct peak near $\sim 90^\circ$, but even for $\lambda \approx 9000 \text{ \AA}$ the peak polarization is only ~ 0.45 . As the wavelength is reduced, the peak polarization declines. For $\lambda \lesssim 6000 \text{ \AA}$, the polarization becomes

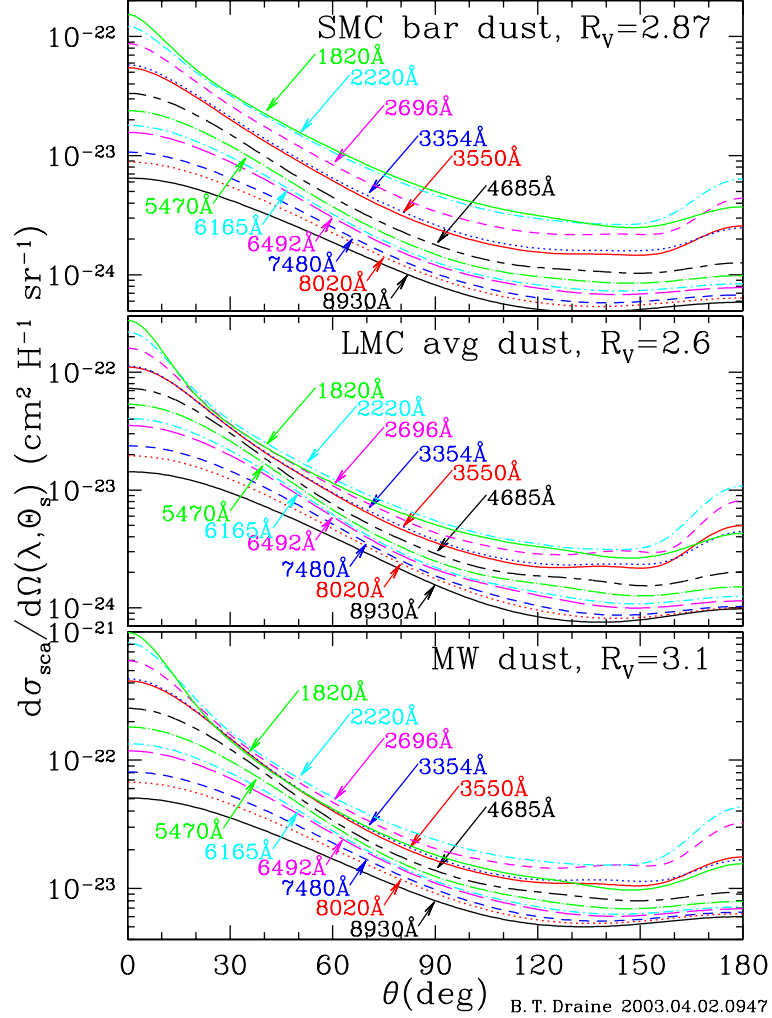


Fig. 6.— $d\sigma_{\text{sca}}/d\Omega$ at selected wavelengths λ , as a function of the scattering angle θ , for WD01 models for Milky Way dust with $R_V = 3.1$, LMC average dust, and SMC bar dust. Curves are labelled by λ .

negative at large scattering angles (see Figure 7), with large negative polarizations in the 120-150° region for $2000 \lesssim \lambda \lesssim 4000 \text{ \AA}$.

Similar results are found for the LMC and SMC dust mixtures – see Fig. 7. Note the very large negative polarizations found for the LMC mixture for $2000 \lesssim \lambda \lesssim 5500 \text{ \AA}$. From the variation of the ultraviolet polarization signature between the different grain size distributions in Figures 7 it is apparent that the ultraviolet polarization is quite sensitive to the details of the grain size distribution.

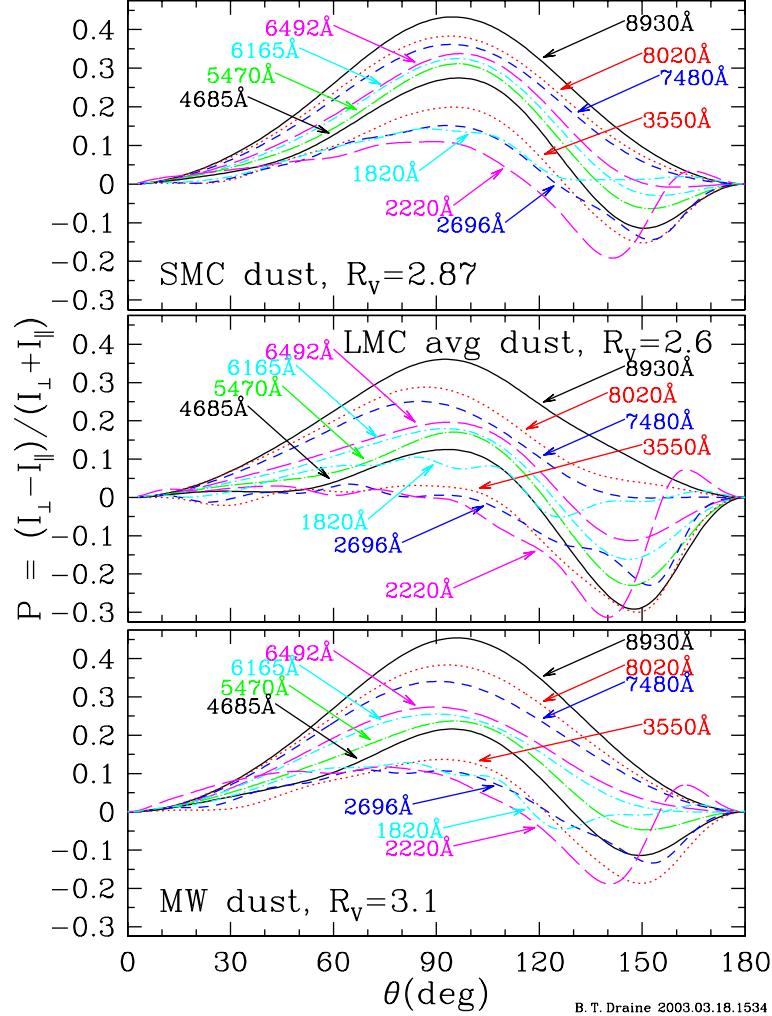


Fig. 7.— Degree of polarization as a function of scattering angle θ , for scattering by Milky Way dust with $R_V = 3.1$, LMC average dust, and SMC bar dust. Curves are labelled by wavelength λ .

3.3. Comparison with Henyey-Greenstein Phase Function

Scattering of unpolarized light by a dust mixture at wavelength λ is characterized by the total scattering cross section per H nucleon, $\sigma_{\text{sca}}(\lambda)$, and a so-called “phase function”

$$\phi(\theta, \lambda) \equiv \frac{4\pi}{\sigma_{\text{sca}}(\lambda)} \frac{d\sigma_{\text{sca}}(\theta, \lambda)}{d\Omega} \quad (8)$$

characterizing the angular distribution of the scattered light, where $d\sigma_{\text{sca}}/d\Omega$ is the differential scattering cross section for unpolarized light. Isotropic scattering would have $\phi = 1$. For anisotropic scattering, one measure of the degree of anisotropy is the “scattering asymmetry factor”

$$g \equiv \langle \cos \theta \rangle = \int \phi(\theta) \cos \theta \frac{d\Omega}{4\pi} = \frac{1}{\sigma_{\text{sca}}} \int_0^\pi \frac{d\sigma_{\text{sca}}}{d\Omega} \cos \theta \ 2\pi \sin \theta d\theta \quad . \quad (9)$$

Henyey & Greenstein (1941) proposed an analytic function to model anisotropic scattering for dust grain mixtures:

$$\phi_{\text{HG}}(\theta) = \frac{1 - g^2}{(1 + g^2 - 2g \cos \theta)^{3/2}} . \quad (10)$$

The Henyey-Greenstein phase function ϕ_{HG} is a convenient analytic form, with a single parameter g , and has been widely used to represent dust scattering properties in radiative transfer calculations in dusty regions.

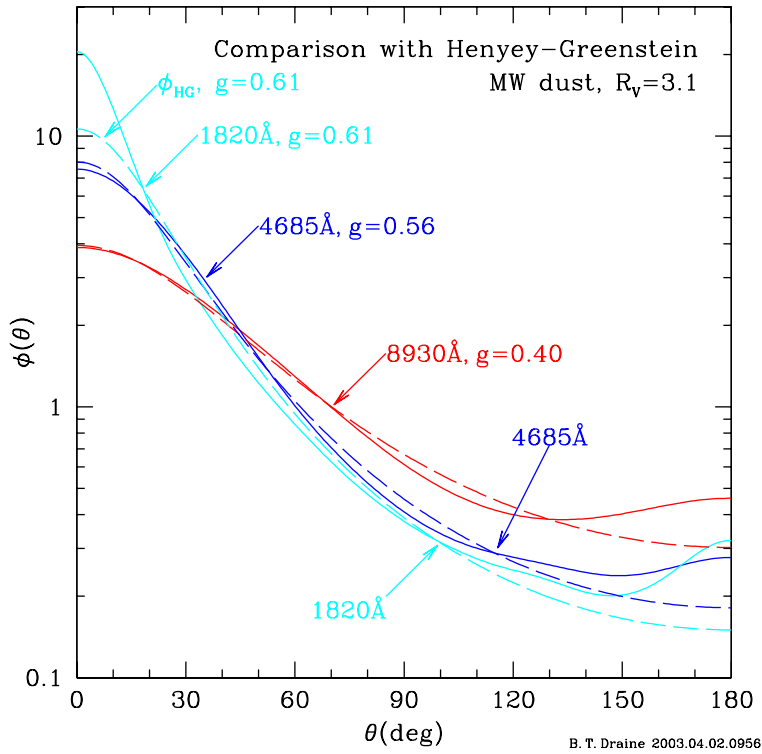


Fig. 8.— Comparison of scattering phase function for the WD01 Milky Way dust model at three wavelengths (solid lines) with the Henyey-Greenstein approximation ϕ_{HG} (eq. 10, broken lines).

By construction, $\phi_{\text{HG}}(\theta)$ has the correct normalization $\int \phi_{\text{HG}}(\theta) d\Omega / 4\pi = 1$ and moment $\langle \cos \theta \rangle = \int \phi_{\text{HG}}(\theta) \cos \theta d\Omega / 4\pi = g$, but ϕ_{HG} of course does not perfectly reproduce the angular dependence of the real phase function $\phi(\theta)$.

How well does ϕ_{HG} approximate $\phi(\theta)$ calculated for realistic dust mixtures? In Figure 8 we show $\phi(\theta)$ calculated at three wavelengths for the WD01 model for Milky Way dust with $R_V = 3.1$, together with the Henyey-Greenstein approximations ϕ_{HG} with the corresponding values of g . For $\lambda = 8930 \text{ \AA}$ and $\lambda = 4685 \text{ \AA}$, the dust is only moderately forward-throwing ($g = 0.40$), and ϕ_{HG} provides a good approximation for scattering angles $\theta < 140^\circ$. It underestimates the backscattering at $\theta > 140^\circ$, but the backscattering is in any case quite weak. At ultraviolet wavelengths, however, the grains become more forward-throwing, and ϕ_{HG} fails to provide a good fit. At $\lambda = 1820 \text{ \AA}$, for

example, we see that $\phi_{\text{HG}}(\theta)$ underestimates the forward scattering by a factor of 2 for $\theta \lesssim 5^\circ$, overestimates the scattering by 20% at $\sim 40^\circ$, and underestimates the scattering by more than 20% for $\theta > 150^\circ$.

To quantify the error associated with use of $\phi_{\text{HG}}(\theta)$ rather than $\phi(\theta)$, we define the r.m.s. relative error

$$h_{\text{rel}} \equiv \left[\int \frac{d\Omega}{4\pi} \left[\frac{\phi_{\text{HG}}(\theta) - \phi(\theta)}{\phi(\theta)} \right]^2 \right]^{1/2}, \quad (11)$$

and r.m.s. absolute error

$$h_{\text{abs}} \equiv \left[\int \frac{d\Omega}{4\pi} [\phi_{\text{HG}}(\theta) - \phi(\theta)]^2 \right]^{1/2}. \quad (12)$$

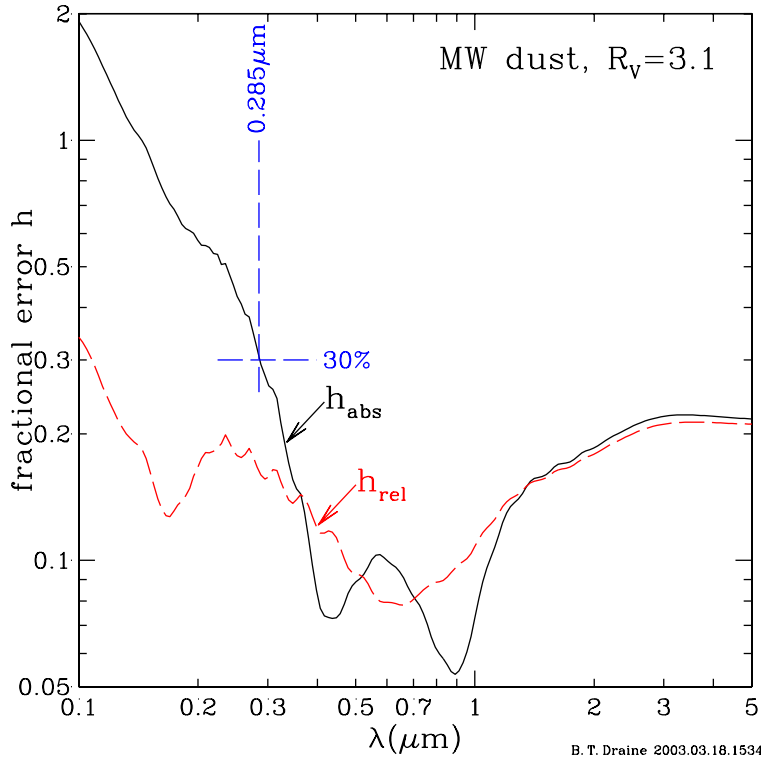


Fig. 9.— Normalized relative error h_{rel} (eq. 11) and absolute error h_{abs} (eq. 12) when the actual phase function $\phi(\theta)$ for the WD01 grain model is approximated by the Henyey-Greenstein phase function ϕ_{HG} (eq. 10).

In the limit of Rayleigh scattering ($\lambda \gg a$),

$$\phi(\theta) \rightarrow \frac{3}{4} (1 + \cos^2 \theta) \quad , \quad (13)$$

for which $g = 0$ and therefore $\phi_{\text{HG}} = 1$. In the Rayleigh limit, ϕ_{HG} has errors

$$h_{\text{abs}} \rightarrow 1/\sqrt{20} \approx 0.22 \quad (14)$$

$$h_{\text{rel}} \rightarrow (13 - 4\pi)^{1/2}/3 \approx 0.22 \quad . \quad (15)$$

The errors h_{rel} and h_{abs} are shown in Figure 9 for the Henyey-Greenstein approximation to the phase function for the WD01 model for Milky Way dust with $R_V = 3.1$. At long wavelengths $\lambda \gtrsim 3\mu\text{m}$, we see that $h_{\text{rel}} \approx h_{\text{abs}} \approx 0.22$, as expected from eq. (14,15). Between ~ 0.4 and $\sim 1\mu\text{m}$, the absolute and relative errors are small, of order 10%, so ϕ_{HG} provides a good approximation to the actual scattering properties. However, we see that the relative and absolute errors exceed 10% for $\lambda \lesssim 4000\text{\AA}$, and become quite large at ultraviolet wavelengths. The absolute error h_{abs} exceeds 50% for $\lambda \lesssim 2200\text{\AA}$. The large absolute error arises because of the very forward-peaked scattering (see Fig. 8): the forward scattering is very strong, with $\phi(0) \gtrsim 10$ for $\lambda \lesssim 2200\text{\AA}$. The Henyey-Greenstein function provides a poor approximation when ϕ is large, resulting in large absolute errors.

In view of the large absolute error $h_{\text{abs}} \gtrsim 0.5$ for $\lambda \lesssim 0.24\mu\text{m}$, we conclude that the Henyey-Greenstein phase function may not be suitable for detailed modeling of reflection nebulae at ultraviolet wavelengths. More complicated parameterizations – such as the use of multiple Henyey-Greenstein phase functions, as by Witt (1977) and Hong (1985) – may be advisable.

3.4. Comparison with Observations

The scattering properties of interstellar dust have been determined observationally by comparing the observed surface brightness of reflection nebulae with model nebulae computed with different dust scattering properties, selecting the model which provides the best match to the observations.

This approach has been used with observations of high surface brightness reflection nebulae (e.g., NGC 2023, NGC 7023, IC 435) illuminated primarily by a single star, and also with observations of the much fainter diffuse galactic light. Figures 10 and 11 show the results so obtained from a number of independent studies, at wavelengths from the optical to vacuum ultraviolet. Also shown are the albedo and asymmetry factor calculated for WD01 grain models representing average Milky Way dust with $R_V \equiv A_V/E(B-V) = 3.1$, and dust from denser regions with $R_V = 4.0$ and 5.5. While there are differences among the different observational determinations, particularly in the ultraviolet, many of the observational results are in general agreement with the albedo and asymmetry factor calculated for the WD01 grain model.

For $\lambda^{-1} < 4\mu\text{m}^{-1}$, the observational studies appear to be in general agreement with one another, but at shorter wavelengths the observational results are sometimes in conflict. For example, from observations of the diffuse galactic light at $\sim 6.25\mu\text{m}^{-1}$ (1600 \AA) Hurwitz et al. (1991) found $(a, g) = (0.185 \pm 0.055, 0.2 \pm 0.2)$, while Witt et al. (1997) found $(a, g) = (0.45 \pm 0.05, 0.68 \pm 0.10)$. There are many factors which could underly such discrepancies – including the difficulty of observations in the vacuum ultraviolet – but given that use of the Henyey-Greenstein phase function introduces an absolute error $h_{\text{abs}} = 70\%$ in the scattering phase function at this wavelength (see Fig. 9), it is possible that reliance on the Henyey-Greenstein approximation may contribute to the disagreements among different observational determinations of the albedo and scattering asymmetry

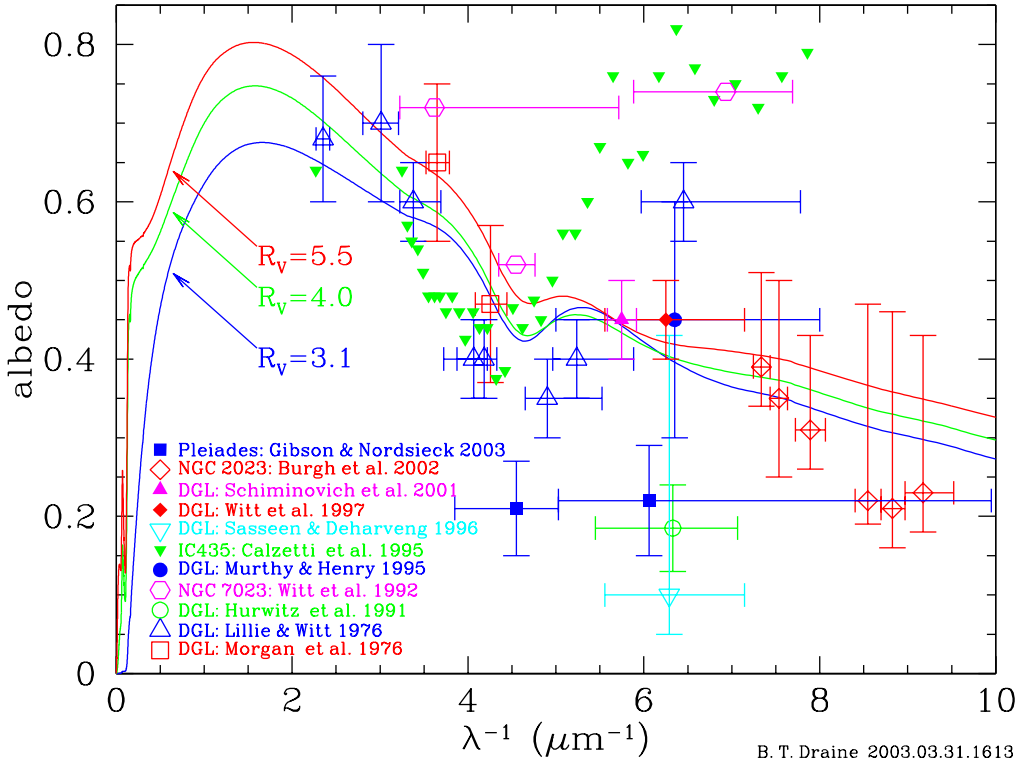


Fig. 10.— Scattering albedo as a function of frequency for different MW dust mixtures, together with observational estimates of the dust albedo in various regions.

in the ultraviolet.

4. Cross Sections for X-Ray Absorption and Scattering

Adopting the dielectric functions discussed in §2, we calculate the scattering and absorption for the WD01 dust grain mixture. We use the Mie scattering theory program of Wiscombe (1980, 1996) for $x = 2\pi a/\lambda < 2 \times 10^4$, and anomalous diffraction theory (van de Hulst 1957) for $x > 2 \times 10^4$. Anomalous diffraction theory provides an excellent approximation at the X-ray energies where $x = 5067(a/\mu\text{m})(E/\text{keV}) > 2 \times 10^4$ (see Figure 7 of Draine & Tan 2003).

The scattering and extinction cross section calculated for the dust mixture is shown in Fig. 12 for 0.1–10 keV X-rays, with the six strongest absorption edges shown in Fig. 13. Also shown is the absorption per H atom due to gas-phase absorption calculated using `phfit2.f` (Verner 1996), with interstellar gas-phase abundances. At energies $13.6 < E \lesssim 250 \text{ eV}$, absorption by neutral H and He is very strong, making it difficult to observe the dust absorption and scattering. Above 250 eV, however, observations of extinction and scattering by dust become feasible for suitably bright sources on sightlines with sufficient dust columns. At $E \gtrsim 800 \text{ eV}$ the extinction is primarily due to dust grains.

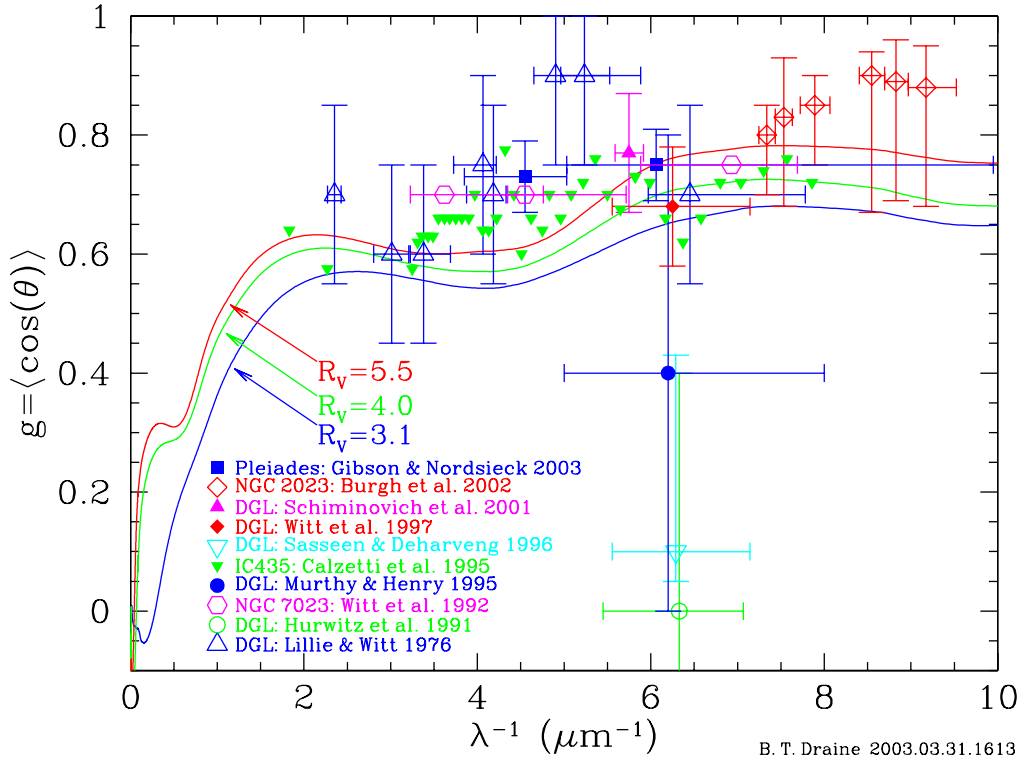


Fig. 11.— Scattering asymmetry factor $g = \langle \cos \theta \rangle$ as a function of frequency for different MW dust mixtures. Also shown are observational estimates for g in various regions.

As seen in Figure 13, the calculated scattering cross sections show conspicuous structure in the vicinity of the major absorption edges. This occurs because at X-ray energies $\text{Re}(\epsilon - 1)$ tends to be negative, and an absorption feature increases $\text{Re}(\epsilon)$ (reducing $|\epsilon - 1|$) just below the absorption feature, and decreases $\text{Re}(\epsilon)$ (increasing $|\epsilon - 1|$) just above the feature. Since the scattering is approximately proportional to $|\epsilon - 1|^2$, this results in a reduction in scattering below an absorption feature, and an increase in scattering above.³ This argument applies to 5 of the 6 absorption edges in Fig. 13; the exception is the C K edge, for which $\epsilon - 1$ actually becomes positive below the absorption edge, with a local peak in scattering just below the K edge.

For the lower-energy absorption edges (C K, O K, Fe L_{2,3}) there is significant variation in the scattering cross section near the absorption edge. As a result, the extinction profile is not the same as the absorption profile. In the case of the O K edge, the extinction peak is at 538.0 eV, whereas the absorption peak is at 537.6 eV. The energy-dependence of the scattering optical depth can be determined by dividing the spectrum of the scattered X-rays by the spectrum of the point source

³Takei et al. (2002) estimate that the dust scattering cross section would be reduced at energies just above the O K edge. We find, to the contrary, that the dust scattering cross section is *increased* just above the O K edge – see Fig. 13.

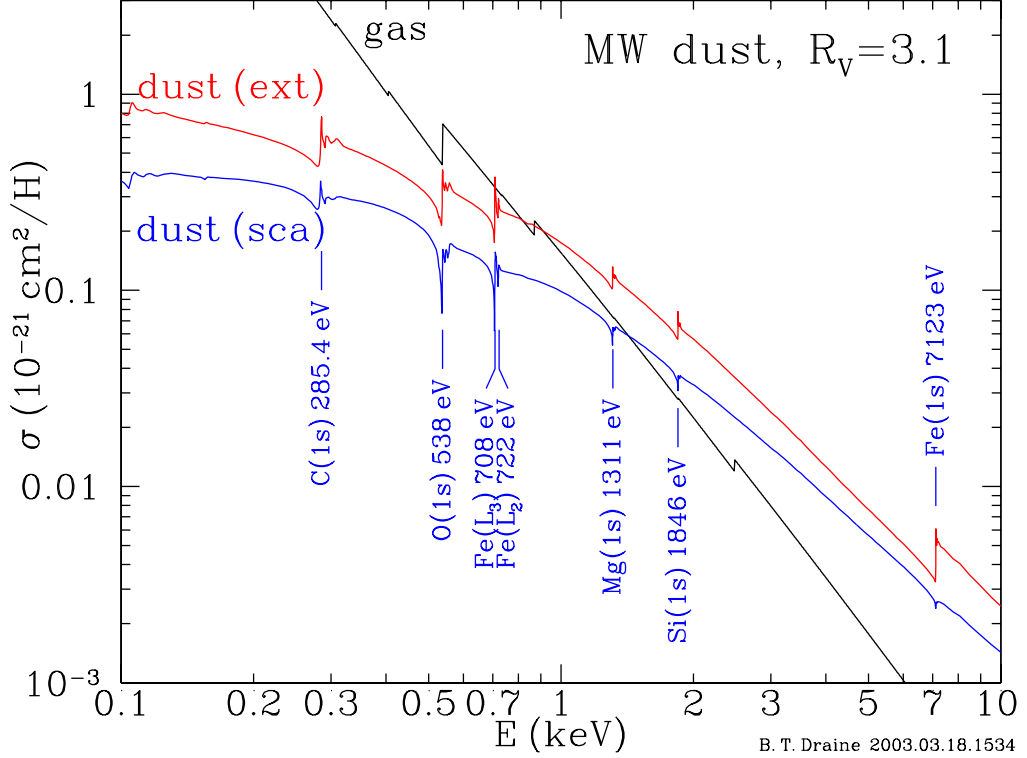


Fig. 12.— X-ray extinction and scattering cross section per H nucleon due to dust.

component. If this can be done with a signal-to-noise ratio $\gtrsim 10$ for ~ 2 eV bins, one should observe the structure in σ_{sca} seen near 285, 538, and 708 eV in Figure 13.

At X-ray energies, the dielectric functions of grain materials become close to unity (see Figures 3 and 5), the wavelength is small compared to the typical grain radius, and the grains are very strongly forward-scattering. The quantity

$$\frac{d\sigma_{\text{sca}}}{d\ln\Omega} = \Omega \frac{d\sigma}{d\Omega} = 2\pi(1 - \cos\theta) \frac{d\sigma}{d\Omega} \approx \pi\theta^2 \frac{d\sigma}{d\Omega} \quad (16)$$

is proportional to the number of scattered photons per logarithmic interval of scattering angle; the location of the peak shows the “typical” scattering angle. Figure 14 shows $\pi\theta^2 d\sigma/d\Omega$ for the WD01 dust mixture for selected energies from 0.3 keV to 10 keV.

Let $\theta_{s,50}(E)$ be the median scattering angle for photons of energy E . Figure 15 shows $\theta_{s,50}(E)$ for the WD01 dust mixture; comparison with Fig. 14 shows that, as expected, the median scattering angle $\theta_{s,50}$ is very nearly the same as the angle where $\pi\theta^2 d\sigma/d\Omega$ peaks. Also shown in Fig. 15 are the 10th and 90th percentile scattering angles, $\theta_{s,10}$ and $\theta_{s,90}$, corresponding to 10% and 90% enclosed power. Note that to a very good approximation,

$$\theta_{s,10} \approx \frac{\theta_{s,50}}{3} \quad \theta_{s,90} \approx 3\theta_{s,50} \quad (17)$$

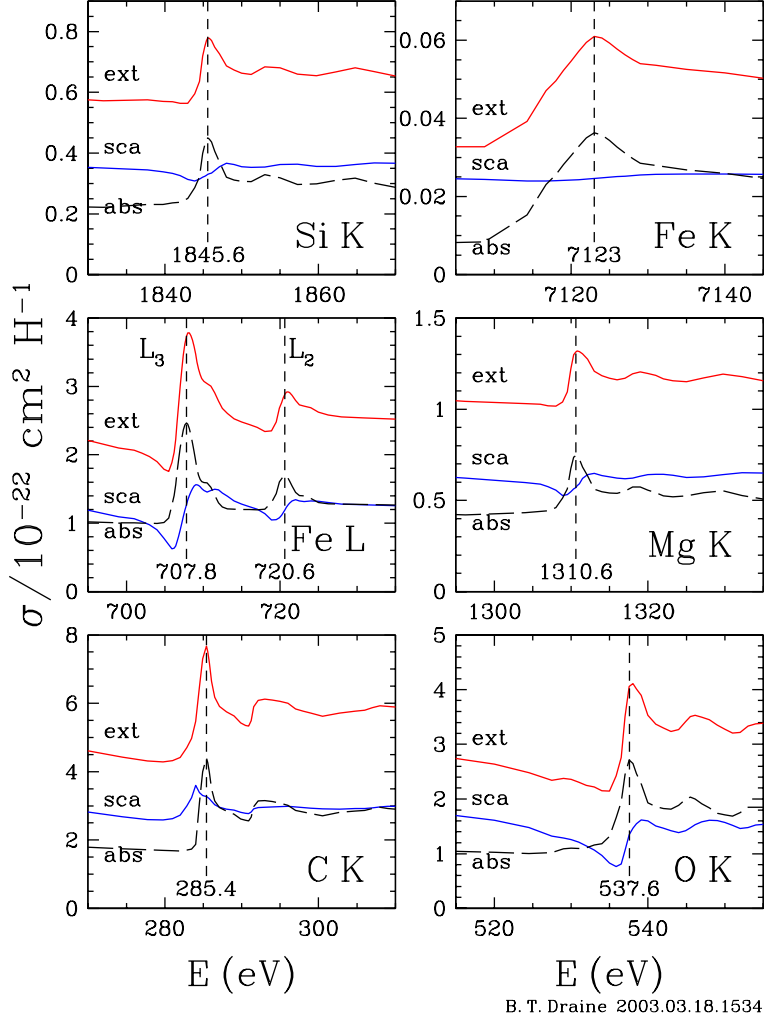


Fig. 13.— X-ray extinction and scattering cross section per H nucleon near major absorption edges.

For $E \gtrsim 0.5$ keV, the median scattering angle for the WD01 dust mixture can be approximated by

$$\theta_{s,50} \approx 360'' \left(\frac{\text{keV}}{E} \right) \quad . \quad (18)$$

The median scattering angle for a circular aperture of diameter d is $0.53\lambda/d$ (Born & Wolf 1999), so equation (18) corresponds to the median scattering angle for an aperture of radius $0.19\mu\text{m}$, consistent with the size of the grains which dominate the visual extinction and polarization of starlight, account for most of the interstellar grain mass, and are expected to dominate the X-ray scattering. The smaller grains, while more numerous, make only a minor contribution to scattering at $E \gtrsim 0.5$ keV. Note that at lower energies, the median scattering angle rises above the approximation (18), due in part to the increasing importance of smaller grains (which contribute most of the geometric cross section of the grain population) at these energies.

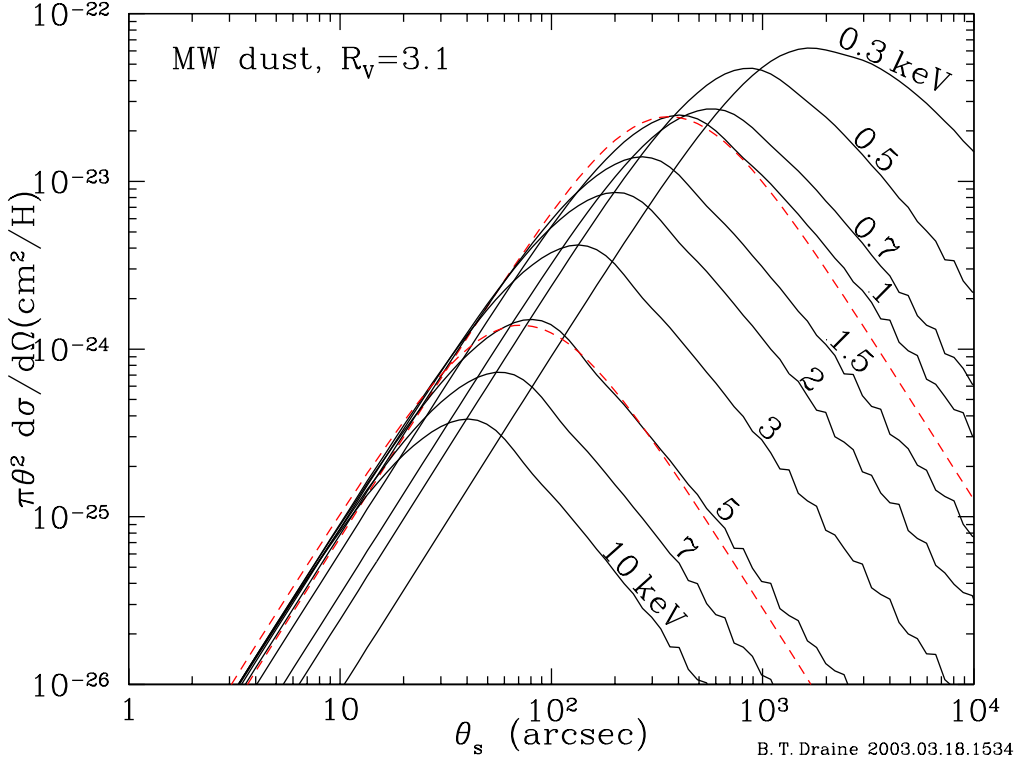


Fig. 14.— $2\pi\theta^2 d\sigma/d\Omega$ versus scattering angle θ_s at selected energies. This function peaks at approximately the median scattering angle. The broken curves show eq. (20) for $E = 1.0$ and 5.0 keV.

For this dust model, the differential scattering cross section can be approximated by the simple analytic form

$$\frac{d\sigma}{d\Omega} \approx \frac{\sigma_{\text{sca}}}{\pi\theta_{s,50}^2} \frac{1}{[1 + (\theta/\theta_{s,50})^2]^2} \quad (19)$$

with the total cross section for scattering angles $< \theta$

$$\sigma_{\text{sca}}(< \theta) = \sigma_{\text{sca}} \frac{(\theta/\theta_{s,50})^2}{1 + (\theta/\theta_{s,50})^2} \quad (20)$$

Eq. (20) reproduces the empirical result that $\theta_{s,10} = \theta_{s,50}/3$, and $\theta_{s,90} = 3\theta_{s,50}$. The approximation (19) is plotted in Fig. 14 for $E = 1.0$ and 5.0 keV, showing that it does indeed provide a good fit.

5. X-Ray Scattering Halos: Models

5.1. Models

For a point source at distance D , scattering by dust on the sightline a distance $r = xD$ from the observer produces a scattered halo around the point source (see, e.g., Draine & Tan 2003) with

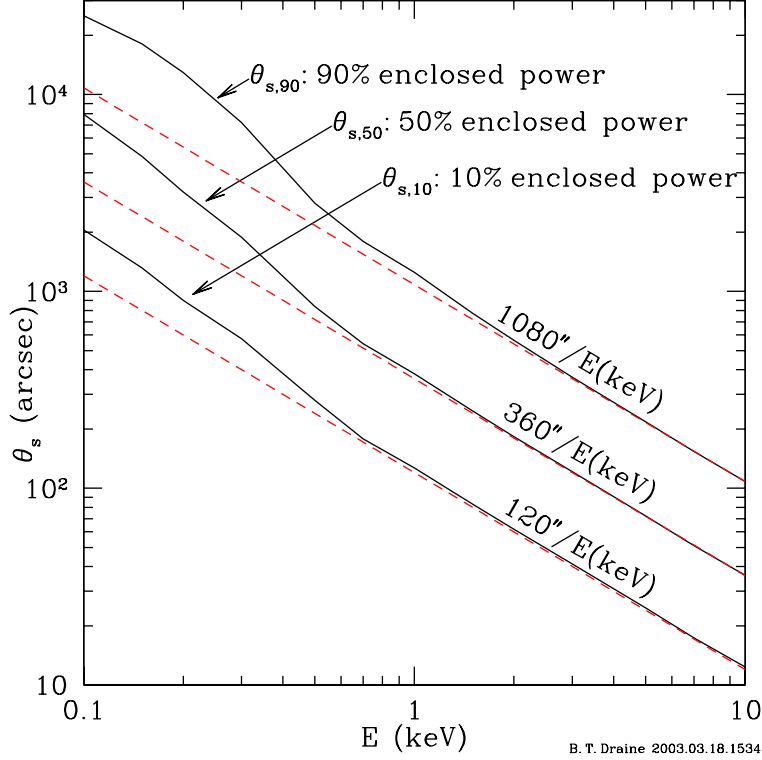


Fig. 15.— Median scattering angle $\theta_{s,50}$ as a function of energy for the WD01 grain model. Also shown are scattering angles $\theta_{s,10}$ and $\theta_{s,90}$ for 10% and 90% enclosed power. Broken lines show asymptotic behavior for $E \gtrsim 1$ keV.

the halo angle θ_h related to the scattering angle θ_s through

$$\theta_h \approx (1 - x)\theta_s \quad (21)$$

Let N_{halo} be the total flux of singly-scattered photons, and $N_{\text{halo}}(< \theta_h)$ be the flux of photons at halo angles $< \theta_h$. Define the fraction of halo photons interior to θ_h

$$g(\theta_h) \equiv \frac{N_{\text{halo}}(< \theta_h)}{N_{\text{halo}}} \quad . \quad (22)$$

If the dust density is assumed to be plane-parallel perpendicular to the sightline, then for the small-angle scattering appropriate to X-ray energies, the scattering halo is given by

$$g(\theta_h) \equiv \int_0^1 dx \tilde{\rho}(x) \frac{\sigma_{\text{sca}}(< \theta_h/(1 - x))}{\sigma_{\text{sca}}} \quad (23)$$

where the dimensionless dust density

$$\tilde{\rho}(x) \equiv \frac{\rho(xD)}{\int_0^1 \rho(xD) dx} \quad (24)$$

where $\rho(r)$ is the dust density along the sightline at distance r from the observer.

Because the differential scattering cross section for the WD01 dust mixture can be approximated by eq. (19,20), we have

$$g(\theta_h) \approx \int_0^1 \tilde{\rho}(x) [1 + (1-x)^2(\theta_{s,50}/\theta_h)^2]^{-1} \quad (25)$$

If the scattering is by a single sheet of dust at distance $x_d D$, then $\tilde{\rho}(x) = \delta(x - x_d)$ and

$$g(\theta_h) \approx \frac{(\theta_h/\theta_{h,50})^2}{1 + (\theta_h/\theta_{h,50})^2} \quad , \quad \theta_{h,50} = (1 - x_d)\theta_{s,50} \quad (26)$$

For a uniform dust density gradient (with $\beta = 0$ corresponding to uniformly-distributed dust)

$$\tilde{\rho}(x) = (1 - \beta) + 2\beta x \quad (-1 \leq \beta \leq 1) \quad (27)$$

eq. (23) can be integrated to obtain

$$g(\theta_h) = (1 + \beta) \frac{\theta_h}{\theta_{s,50}} \arctan(\theta_{s,50}/\theta_h) - \beta \left(\frac{\theta_h}{\theta_{s,50}} \right)^2 \ln [1 + (\theta_{s,50}/\theta_h)^2] \quad ; \quad (28)$$

$g(\theta_h)$ is plotted in Fig. 16 for 5 cases: $\beta = -1$ (1/4 of the dust between $x = 0.5$ and 1); $\beta = -.5$ (3/8 of the dust between $x = 0.5$ and 1); $\beta = 0$ (uniform dust); $\beta = 0.5$ (5/8 of the dust between $x = 0.5$ and 1); $\beta = 1$ (3/4 of the dust between $x = 0.5$ and 1). Also plotted is the case where the dust is all at $x \ll 1$, with $\theta_h = \theta_s$. For the above dust distributions, Table 2 gives the halo angles $\theta_{h,10}$, $\theta_{h,50}$, $\theta_{h,90}$ enclosing 10%, 50%, and 90% of the halo power for single-scattering.

Table 2: Halo Structure Parameters for WD01 Dust

	dust density distribution				
	$\beta = -1$	$\beta = -0.5$	uniform	$\beta = 0.5$	$\beta = 1$
$\theta_{h,10}/\theta_{s,50}$	0.1663	0.1032	.0664	.0467	.0353
$\theta_{h,50}/\theta_{s,50}$	0.631	0.530	0.429	0.337	0.262
$\theta_{h,90}/\theta_{s,50}$	2.084	1.882	1.660	1.413	1.139
$\theta_{h,10}(E/\text{keV})$	59.9''	37.2''	23.9''	16.8''	12.7''
$\theta_{h,50}(E/\text{keV})$	227''	191''	154''	121''	94.3''
$\theta_{h,90}(E/\text{keV})$	750''	678''	598''	509''	410''

6. X-Ray Scattering Halos: Observations

The total cross section for X-ray scattering can be measured by imaging the scattered X-ray halo. The flux of scattered photons, N_{halo} , is related to the flux in the point-source component, N_{ptsr} , by $N_{\text{ptsr}} = (N_{\text{ptsr}} + N_{\text{halo}}) \exp(-\tau_{\text{sca}})$, so

$$\tau_{\text{sca}} = \ln(1 + N_{\text{halo}}/N_{\text{ptsr}}) = -\ln(1 - f_{\text{halo}}) \quad , \quad (29)$$

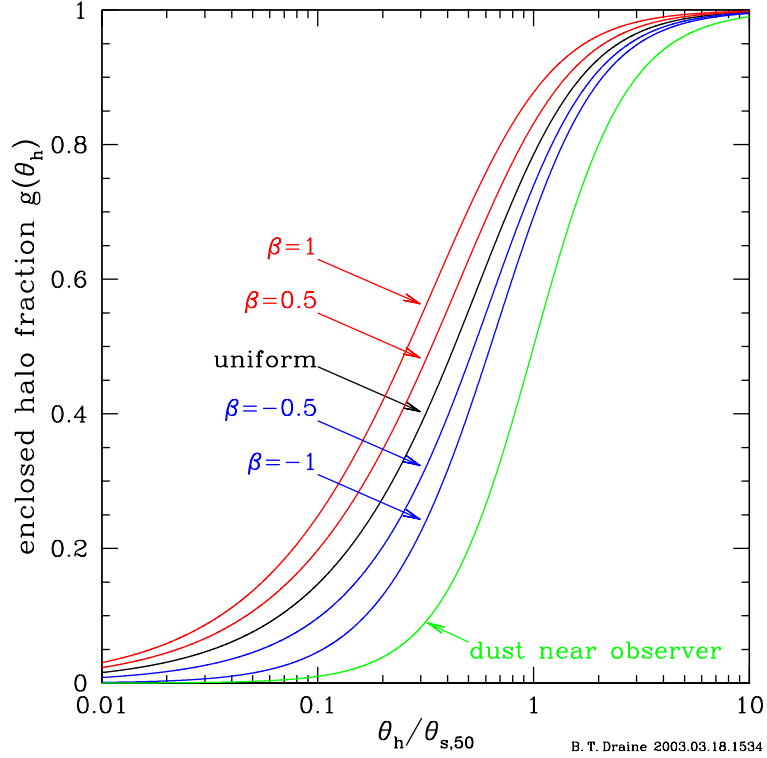


Fig. 16.— Fraction of the single-scattering halo falling within halo angle θ_h , as a function of $\theta_h/\theta_{s,50}$, where $\theta_{s,50}$ is the median scattering angle.

$$f_{\text{halo}} \equiv \frac{N_{\text{halo}}}{N_{\text{halo}} + N_{\text{ptsrc}}} ; \quad (30)$$

eq. (29) is valid even when multiple scattering takes place. Absorption (by dust or gas) has a negligible effect on $N_{\text{halo}}/N_{\text{ptsrc}}$, because unscattered and scattered photons are affected essentially equally. Estimation of τ_{sca} from (29) requires determination of the flux of scattered photons N_{halo} integrated over all halo angles. If the halo flux is measured only for halo angles $\theta_1 < \theta_h < \theta_2$, the total halo flux can be estimated from

$$N_{\text{halo}} = \frac{N_{\text{halo}}(\theta_1 < \theta_h < \theta_2)}{g(\theta_2) - g(\theta_1)}; \quad (31)$$

the function $g(\theta_h)$ of course depends on assumptions both concerning the grain model and the distribution of dust along the sightline.

6.1. Cen X-3

Woo et al. (1994) used the *ASCA* X-ray observatory to measure the X-ray halo toward the massive X-ray binary Cen X-3 ($A_V \approx 4.3$) as a function of orbital phase, at 1.5 and 2.5 keV. Their

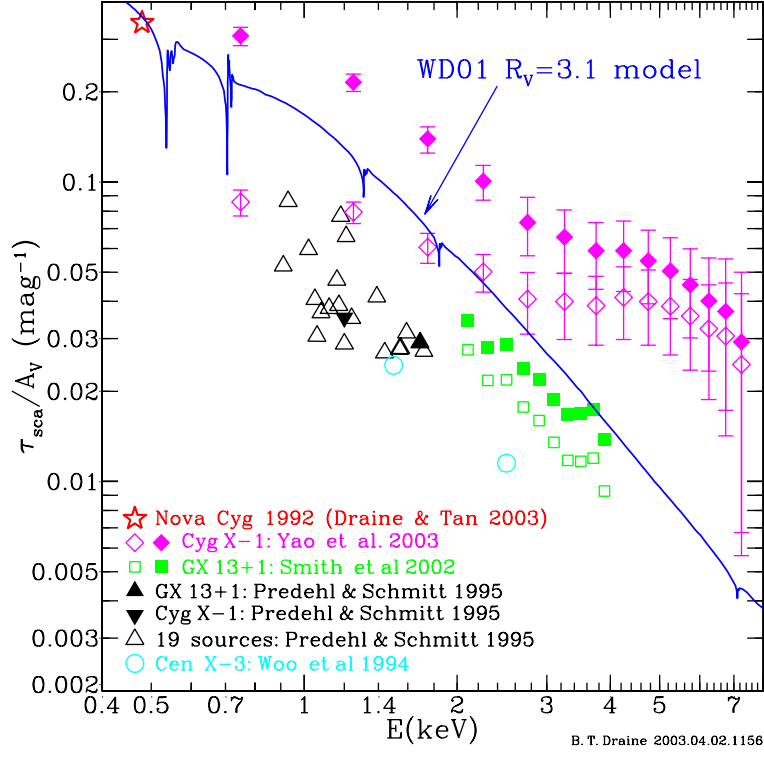


Fig. 17.— Scattering optical depth τ_{sca} per unit visual extinction A_V as calculated for the WD01 model (solid line) and as estimated from various observations (see text). *Chandra* imaging of GX 13+1 at $50'' < \theta_s < 600''$ (Smith, Edgar, & Shafer 2002) has been corrected for photons interior to $50''$ assuming uniformly distributed dust (open squares) or dust with density proportional to distance (filled squares). *Chandra* observations of Cyg X-1 at $\theta_s < 60''$ (Yao et al. 2003) are uncorrected for photons beyond $60''$ (open diamonds) or corrected assuming uniform dust (filled diamonds). See text.

results for τ_{sca}/A_V are shown in Figure 17. Also shown is the ratio τ_{sca}/A_V estimated for the WD01 grain model. Woo et al.’s values of τ_{sca}/A_V at 1.5 and 2.5 keV are a factor ~ 3.5 below the prediction of the WD01 grain model. Can we understand this?

At 1.5 keV, the ASCA point spread function was such that even when the point source component was at a minimum, the halo intensity exceeded the point source intensity only for $\theta_h > 200''$; when the point source was at maximum the halo intensity exceeded the point source intensity only for $\theta_h \gtrsim 450''$. For uniformly-distributed dust and $E = 1.5$ keV, we expect a median halo angle $\theta_{h,m} \approx 100''$ (see Table 2); it is therefore clear that the ASCA observations were insensitive to most of the scattered photons. It therefore seems plausible that the scattered flux may have been underestimated by factors of 2-4 due to the dominance of the point source profile at halo angles $\theta \lesssim 200 - 400''$. The determination of τ_{sca}/A_V by Woo et al. should be treated as a lower bound rather than a measurement.

6.2. *ROSAT* Observations

ROSAT observed both unscattered and scattered X-rays from Nova Cygni 1992 at a number of epochs (Krautter et al. 1996). The most recent reanalysis of the *ROSAT* data found $\tau_{\text{sca}} = 0.211 \pm 0.006$ at the median photon energy ~ 480 eV (Draine & Tan 2003). Adopting $E(B - V) = 0.19$ estimated from observations of $\text{H}\alpha/\text{H}\beta$ (Barger et al. 1993; Mathis et al. 1995), we obtain $\tau_{\text{sca}}/A_V = 0.36$. As seen in Figure 17, this value is in excellent agreement with the WD01 grain model. Draine & Tan have also carried out detailed modelling, and conclude that the observed X-ray halo profiles at 9 different epochs are in good agreement with the WD01 dust model.

Predehl & Schmitt (1995, hereafter PS95) used *ROSAT* to estimate f_{halo} for Cyg X-1, GX 13+1, and 19 other galactic sources for which A_V was also available. In each case, PS95 have fitted the observations with the *ROSAT* psf plus a theoretical dust model, and used this to estimate the total number of scattered photons. Figure 17 shows the resulting τ_{sca}/A_V versus the average photon energy for each source. The estimates of τ_{sca}/A_V inferred from the PS95 observations are generally a factor $\sim 2 - 4$ below the WD01 grain model. If the PS95 values of f_{halo} are accurate, this would indicate a serious problem with the WD01 grain model.

However, for the 21 sources, the halo angle at which the intensities of the fitted halo and psf were equal was $70''$ or larger; for 50% of the sources this angle was $130''$ or larger. At a typical energy of ~ 1.2 keV, the median scattering angle is $\theta_{h,50} \approx 130''$ for uniformly-distributed dust (see Table 2). Estimates of f_{halo} therefore rely heavily on the dust model to separate the halo from the point source at small halo angles. The modelling by PS95 employed power-law grain size distributions $dn/da \propto a^{-q}$ for $a < a_{\text{max}}$. For the 21 sources, the median q value was 4.0 and the median value of a_{max} was $0.18\mu\text{m}$. Power-law grain size distributions with $q \approx 3.5$ and $a_{\text{max}} \approx 0.25\mu\text{m}$ (Mathis, Rumpl, & Nordsieck 1977; Draine & Lee 1984) provide a good fit to the interstellar extinction, but the size distributions adopted by PS95 – with generally steeper power laws and smaller values of a_{max} – had insufficient mass in large grains⁴ and do not provide a good fit to the extinction law. The scattering at small halo angles is dominated by the larger grains, so the PS95 model-fitting appears to have systematically underestimated the actual halo intensity at small halo angles.

Given likely uncertainties in the psf and the model-fitting, it seems likely that the PS95 values of τ_{sca}/A_V are systematically low, perhaps by factors as large as 2-4. We now examine two particular sightlines.

⁴The median $q = 4.0$ corresponds to equal mass per logarithmic interval; for $q \geq 4.0$ the grain mass diverges at small radii unless a lower cutoff is imposed.

6.3. GX 13+1

GX 13+1 is a low-mass X-ray binary system at $l = 13.5^\circ$, $b = 0.10^\circ$, and an estimated distance $D \approx 7$ kpc, corresponding to a distance above the plane $D \sin b \approx 12$ pc. Garcia et al. (1992) estimated $A_V \lesssim 14.4$. X-ray spectroscopy gives $N_H = 2.9 \pm 0.1 \times 10^{22} \text{ cm}^{-2}$ (Ueda et al. 2001), corresponding to $A_V = 15.5$ for the standard conversion $N_H/A_V = 1.87 \times 10^{21} \text{ cm}^{-2}$ (Bohlin, Savage, & Drake 1978). We adopt $A_V = 14$. The mean photon energy for the *ROSAT* observations is $E = 1.69 \text{ keV}$ (PS95).

PS95 find a halo fraction $f_{\text{halo}} = 0.335$ for GX 13+1, but this may be an underestimate:

- For GX 13+1, PS95 estimate that the halo and psf have equal intensities at $\sim 75''$ (see their Fig. 10).⁵ For uniformly-distributed dust and $E = 1.69 \text{ keV}$, the median halo angle $\theta_{h,50} \approx 91''$, but on this sightline the dust density may be enhanced closer to the source, leading to a reduction in $\theta_{h,50}$; for a linear gradient with $\beta = 1$, $\theta_{h,50} \approx 58''$. Thus it appears possible that $\gtrsim 50\%$ of the scattered photons may have been misattributed to the psf.⁶
- For GX 13+1, PS95 used a dust model with $dn/da \propto a^{-3.8}$ and $a_{\text{max}} = 0.18 \mu\text{m}$; as discussed above, this underestimates the abundances of $a \gtrsim 0.1 \mu\text{m}$ grains, and therefore underestimates the contribution of scattering at small halo angles.

It therefore appears that PS95 could have underestimated N_{halo} . While difficult to quantify, it seems possible that the true value of f_{halo} might be as large as 0.65 (the value predicted by the WD01 grain model for $E = 1.69 \text{ keV}$ and $A_V = 14$).

The X-ray halo around GX 13+1 has recently been observed by the *Chandra* X-ray telescope (Smith, Edgar, & Schafer 2002) at energies between 2.1 and 3.9 keV, with energy resolution $\sim 0.2 \text{ keV}$. Phenomena referred to as “pileup” and “grade migration” in the detection system affect the *Chandra* ACIS images as far as $50''$ from the source. Smith et al. also discuss the current uncertainties concerning the *Chandra* psf at angles $> 50''$. Using a preliminary psf based on observations of Her X-1, they estimate what they refer to as “total observed halo fraction” $I(E)$ by integrating the psf-subtracted and background-subtracted count rates from $50''$ to $600''$, and dividing by the estimated total count rate (point source + halo) in the absence of saturation effects. If we assume a model for the dust distribution, we can estimate the total scattering optical

⁵The *ROSAT* psf fit given by Boese (2000) has 90%-enclosed-power radii of $32''$ at 0.5 keV , $25.5''$ at 1 keV , $35''$ at 1.5 keV , $52''$ at 1.69 keV , and $95''$ at 2.0 keV . It is not clear how close the actual psf is to the fit given by Boese.

⁶The *ROSAT* imaging extends to $\theta_h \approx 2000''$, but for GX 13+1 the background is estimated to exceed the halo intensity for $\theta_h \gtrsim 900''$; determination of the background is itself difficult, and underestimation of N_{halo} due to background oversubtraction at $\theta \gtrsim 600''$ is an additional possibility. However, since 90% of the scattering at 1.69 keV is at scattering angles $\lesssim 1080''/1.69 = 640''$, underestimation of the halo intensity at $\theta_h > 600''$ would have only a small effect on N_{halo} .

depth

$$\tau_{\text{sca}} = \ln \left[1 + \frac{I}{(1-I)} \frac{1}{[g(600'') - g(50'')]} \right] , \quad (32)$$

where $g(\theta_h)$ is given by eq. (28). In Figure 17 we show the values of τ_{sca}/A_V obtained from the observed I , with $g(\theta_h)$ calculated for the WD01 grain model assuming (a) uniformly-distributed dust ($\beta = 0$) and (b) dust with a density gradient $\beta = 1$.

The best way to use the information in the observed scattered halo is to try to reproduce the observed radial profile of the scattered halo using a dust model, and Smith et al. tested various grain models in this way. For dust distributed uniformly between source and observer, for the WD01 grain model they find a best-fit gas column $N_{\text{H}} = 1.65 \times 10^{22} \text{ cm}^{-2}$, significantly smaller than the value $2.9 \pm 0.1 \times 10^{22} \text{ cm}^{-2}$ estimated from *ASCA* observations (Ueda et al. 2001). Note, of course, that additional dust could be located at $x > 0.75$ without appreciably affecting the observed $I_{>50''}$ since the additional halo contribution would be mainly below the $50''$ lower cutoff.⁷

6.4. Cygnus X-1

Cygnus X-1 consists of an O star primary with a black hole companion (see Tanaka & Lewin 1995), located at $l = 71.33^\circ$, $b = 3.07^\circ$, and an estimated distance $D = 2.5 \pm 0.4 \text{ kpc}$ (Bregman et al. 1973; Ninkov et al. 1986), placing it at a height $D \sin b \approx 130 \pm 20 \text{ pc}$ above the plane. The O9.7 Iab primary is reddened by $E(B-V) = 1.12$ (Bregman et al. 1973), corresponding to $A_V = 3.5$; this is consistent with $N_{\text{H}} = 6.2 \times 10^{21} \text{ cm}^{-2}$ from X-ray absorption spectroscopy (Schulz et al. 2002). Based on studies of reddening vs. distance for stars within $50'$ of Cyg X-1 (Bregman et al. 1973; Margon et al. 1973) it appears that the dust is distributed approximately uniformly along the sightline.

PS95 observed Cygnus X-1 with *ROSAT*, and found $f_{\text{halo}} = 0.116$ at 1.2 keV. The psf and scattered halo intensity were estimated to be equal at $\theta \approx 110''$. The PS95 result $\tau_{\text{sca}}/A_V = .037 \text{ mag}^{-1}$ at 1.2 keV is a factor 3 below the WD01 model (see Fig. 17).

Yao et al. have recently used *Chandra* observations of Cygnus X-1 to infer the scattered halo, using a technique designed to minimize the effects of “pileup”, allowing the excellent angular resolution of *Chandra* to be used to observe at small halo angles. Yao et al. neglected halo angles $\theta > 60''$, but were able to measure the halo as close as $1''$ from the point source.

Yao et al. also report the radius θ_* containing 50% of the halo counts within $60''$ of the source, i.e., $g(\theta_*) = 0.5g(60'')$. In Figure 18 we show the variation of θ_* with E calculated for two dust distributions: uniform dust, and a thin sheet at $x_d = 0.89$. The uniform dust model is in approximate overall agreement with the distribution of halo counts within $60''$, although it does

⁷ $\theta_{h,m} = 43''$ for $E = 2.1 \text{ keV}$ and dust at $x_d = 0.75$.

not reproduce the extreme concentration of the halo at $E \approx 2$ keV found by Yao et al. While the small values of θ_* can be reproduced by a model with dust at a single distance $x_d \approx 0.89$, such a dust distribution does not seem appropriate for this sightline, and would also be inconsistent with the values of θ_* reported for $E \gtrsim 3.5$ keV.

Adopting the uniform dust model, we can now use the WD01 model to correct for halo counts at $\theta_h > 60''$: $\tau_{\text{sca}} = \ln[1 + N_{\text{halo}}(< 60'')/g(60'')]$, with the results plotted in Fig. 17.

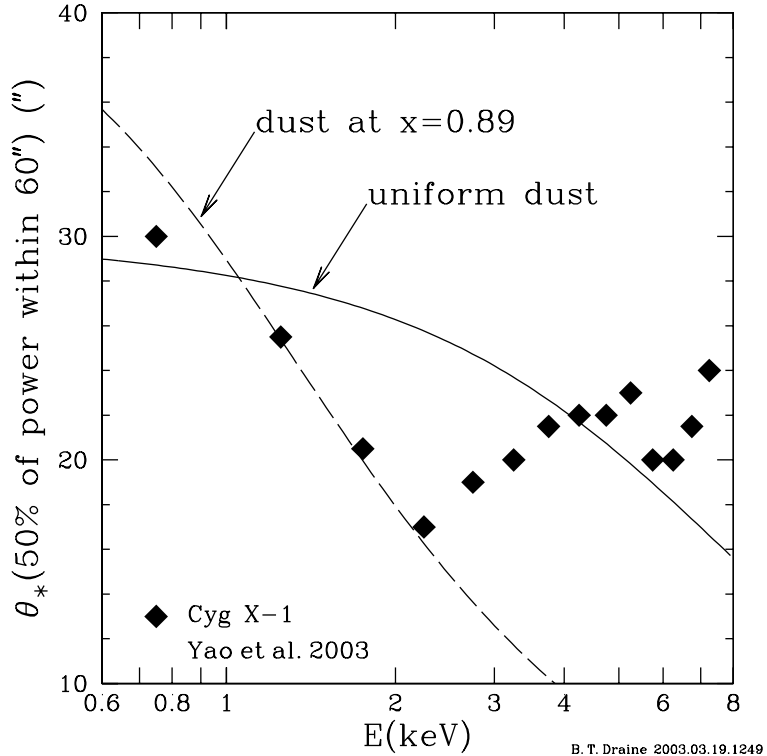


Fig. 18.— Radius θ_* enclosing 50% of the halo counts within $60''$ of the point source. Data points are observations of Cyg X-1 by Yao et al. (2003).

At $E < 2.5$ keV, where the estimated fractional uncertainties are smallest, the values of τ_{sca}/A_V found from the Yao et al. results fall a factor $\sim 1.5 - 2$ above the predictions of the WD01 model. The reason for this is not apparent, but we speculate that perhaps the point source flux has been underestimated.

At $E \gtrsim 2.5$ keV, however, the inferred value of τ_{sca}/A_V departs increasingly from the WD01 dust model, with discrepancies as large as a factor ~ 7 at $5 - 7$ keV. It is very difficult to envision a dust model which could have such a large value of τ_{sca}/A_V at these energies, so we presume that the observations are affected by some systematic error – perhaps the *Chandra* psf at these energies may have been underestimated, or the novel method employed by Woo et al to reconstruct the radial profile may be prone to systematic errors which are not fully understood.

6.5. Discussion

We have reviewed a number of measurements of dust scattering halos, and compared the predictions of the WD01 grain model to the values of τ_{sca}/A_V estimated from these observations. The results, shown in Fig. 17, are equivocal. Two studies (Woo et al. 1994; Predehl & Schmitt 1995) find values of τ_{sca}/A_V much lower than expected for the WD01 dust model, but we give arguments why these observations might have substantially underestimated the total halo flux. *Chandra* observations of GX 13+1 by Smith et al. (2002), after correcting for missed halo counts using the constant dust gradient model with $\beta = 1$, are within a factor ~ 2 of the WD01 model, but it is clear that the corrections are sensitive to the (unknown) dust density distribution for this case, since the halo intensity was not measured at $\theta_h < 50''$.

The recent *Chandra* measurement of the halo around Cyg X-1 (Yao et al. 2003) implies values of τ_{sca}/A_V which are a factor ~ 2 larger than expected for the WD01 model at energies $E < 2.5$ keV, but the derived values of τ_{sca} require correction for halo photons at $60''$, and are sensitive to assumptions concerning the spatial distribution of the dust. At higher energies, $E \gtrsim 4$ keV the corrections become small, but the values of τ_{sca}/A_V exceed the WD01 model by large factors.

It should be noted that Draine & Tan (2003) have quantitatively modelled the observed X-ray halo around Nova Cygni 1992 using the WD01 grain model. The observed X-ray halo intensity can be reproduced using a dust column density which agrees with the reddening inferred from the observed H α /H β intensity ratio. This suggests that the WD01 grain model, with the X-ray scattering properties calculated here, may be consistent with observations – the points in Fig. 17 which fall well below the WD01 model curve may be attributable to observational underestimates of the halo intensity at small angles. The fact that the *Chandra* observations of Cyg X-1 at 1.25 and 1.75 keV (Yao et al. 2003) find a scattered halo of the expected total strength suggests that the WD01 model may in fact be consistent with X-ray observations at these higher energies as well as the ~ 0.5 keV *ROSAT* observations of Nova Cygni 1992.

It is hoped that future *Chandra* observations will be able to carry out high-signal-to-noise observations of X-ray scattering halos on sightlines where the dust distribution and reddening are well-determined. An optimal situation for this would be to use a source which is known to be distant compared to the dust doing the scattering, so that we can assume that $x \lesssim 0.2$ in eq. (21). An extragalactic X-ray point source (AGN or quasar) would be ideal for this purpose.

7. Summary

The following are the principal results of this work:

1. Dielectric functions for graphite and MgFeSiO₄ have been constructed which are continuous from submm to hard X-rays, obey the Kramers-Kronig relations, and satisfy the oscillator strength sum rule.

2. Differential scattering cross sections at optical and ultraviolet wavelenghts have been calculated at selected wavelengths for dust mixtures appropriate to the diffuse interstellar medium in the Milky Way, the LMC, and the SMC. These scattering functions, which can be used for modelling reflection nebulae, are available at <http://www.astro.princeton.edu/~draine> .
3. The polarization of scattered light, as a function of scattering angle, is calculated at selected wavelengths.
4. The calculated phase functions are compared to the widely-used Henyey-Greenstein phase function. At wavelengths $0.4\mu\text{m} \lesssim \lambda \lesssim 1\mu\text{m}$, the calculated phase function can be fitted to within $\sim 10\%$ by the Henyey-Greenstein phase function. In the ultraviolet, however, the Henyey-Greenstein phase function provides a poor fit, with absolute errors exceeding 50% at $\lambda < 2400\text{\AA}$. The Henyey-Greenstein phase function may not be suitable for quantitative modelling of reflection nebulae in the ultraviolet. Use of this phase function may contribute to discrepancies between different observational estimates of the albedo a and scattering asymmetry factor $g = \langle \cos \theta \rangle$ in the vacuum ultraviolet.
5. Absorption, scattering, and extinction have been calculated for the WD01 grain model at X-ray energies. The calculated absorption edge structure appears to be consistent with recent spectroscopy by the *Chandra X-Ray Observatory*, and can be further tested by future observations.
6. Differential scattering cross sections are presented for the Milky Way dust model at X-ray energies. These can be used for modelling X-ray scattering halos, and are available at <http://www.astro.princeton.edu/~draine> .
7. The median scattering angle $\theta_{s,50}(E)$ is given, as well as the scattering angles $\theta_{s,10}$ and $\theta_{s,90}$ for 10% and 90% enclosed power. These can be used to assess the sensitivity of imaging observations for determination of the flux of halo photons.
8. Simple analytic functions provide a good approximation to the differential scattering cross section for dust (eq. 19,20).
9. We provide analytic approximations to $g(\theta_h)$, the fraction of the halo counts interior to θ_h , for dust in a single sheet (eq. 26) and uniformly-distributed dust or dust with a density gradient (eq. 28).
10. The total scattering cross section calculated for the WD01 grain model is compared with observations of X-ray halos by *ASCA*, *ROSAT*, and *Chandra* (see Fig. 17). The results are somewhat equivocal, and in some cases depend on corrections which are sensitive to the spatial distribution of the dust. The cross sections for X-ray scattering which are inferred from the observations fall both above and below the WD01 model. At this point we can only conclude that the WD01 model is not rejected by existing data.

11. Analysis of the angular structure of X-ray halos around Galactic sources will generally be compromised by uncertainties concerning the location of the dust responsible for the scattering. The ideal observation is to observe an extragalactic point source, in which case the scattering dust is all at $x \approx 0$. It is hoped that such observations will be carried out by *Chandra* or *XMM* for bright extragalactic sources located behind sufficient Galactic dust, thereby providing a definitive test of this and other dust models.

I thank Jonathan Tan and Adolf Witt for helpful discussions, and Robert Lupton for making available the SM software package. This work was supported in part by NSF grant AST-9988126.

REFERENCES

Altarelli, M., Dexter, D.L., Nussenzveig, H.M., & Smith, D.Y. 1972, Phys. Rev. B, 6, 4502

Barger, A.J., Gallagher, J.S. III, Bjorkman, K.S., Johansen, K.A., & Nordsieck, K.H. 1993, ApJ, 419, L85

Bohlin, R.C., Savage, B.D., & Drake, J.F. 1978, ApJ, 224, 132

Bohren, C.F., & Huffman, D.R. 1983, Absorption and Scattering of Light by Small Particles (New York: Wiley)

Boese, F.G. 2000, A&AS, 141, 507

Born, M., & Wolf, E. 1999, Principles of Optics, 7th ed. (Cambridge: Cambridge Univ. Press) §8.5.2

Bregman, J., Butler, D., Kemper, E., Koski, A., Kraft, R.P., & Stone, R.P.S. 1973, ApJ, 185, L117

Burgh, E.B., McCandliss, S.R., & Feldman, P.D. 2002. ApJ575:240-49

Calzetti, D., Bohlin, R.C., Gordon, K.D., Witt, A.N., & Bianchi, L. 1995. ApJ, 446, L97

Djurisic, A., & Li, E.H. 1999, J. Appl. Phys., 85, 7404

Draine, B.T. 2003, ARAA, 41, 000

Draine, B.T., & Lee, H.-M. 1984, ApJ, 468, 269 (DL84)

Draine, B.T., & Li, A. 2001, ApJ, 551, 807

Draine, B.T., & Malhotra, S. 1993, ApJ, 414, 632

Draine, B.T., & Tan, J.C. 2003, ApJ, submitted [<http://arxiv.org/abs/astroph/0208302>]

Dufour, R.J. 1984, in IAU Symp. 108, Structure and Evolution of the Magellanic Clouds, ed. S. van den Bergh & K.S. de Boer (Dordrecht: Reidel) 353

Fitzpatrick, E.L. 1985, *ApJ*, 299, 219

Fitzpatrick, E.L. 1986, *ApJ*, 92, 1068

Garcia, M.R., Grindlay, J.E., Bailyn, C.D., Pipher, J.L., Shure, M.A., & Woodward, C.E. 1992, *AJ*, 103, 1325

Garvie, L.A.J., Rez, P., Alvarez, J.R., Buseck, P.R., Craven, A.J., & Brydson, R. 2000, *American Mineralogist*, 85, 732

Gibson, S.J., & Nordsieck, K.H. 2003, *ApJ*, preprint doi:10.1086/374590

Gordon, M.L., Tulumello, D., Cooper, G., Hitchcock, A.P., Glatzel, P., Mullins, O.C., Cramer, S.P., & Bergmann, U. 2003, submitted to *J. Phys Chem B*

Hayakawa, S. 1973, in Interstellar Dust and Related Topics, IAU Symposium No. 52, ed. J.M. Greenberg & H.C. van de Hulst (Dordrecht: Reidel), p. 283

Henderson, C.M.B., Cressey, G., & Redfern, S.A.T. 1995, *Radiat. Phys. Chem.* 45, 459

Henyey, L.G., & Greenstein, J.L. 1941, *ApJ*, 93, 70

Hong, S.S. 1985, *A&A*, 146, 67

Hurwitz, M., Bowyer, S., & Martin, C. 1991, *ApJ*, 372, 167

Kim, S.-H., & Martin, P.G. 1995, *ApJ*, 442, 172

Koornneef, J. 1982, *A&A*, 107, 247

Krautter, J., Ögelman, H., Starrfield, S., Wichmann, R., & Pfeffermann, E. 1996, *ApJ*, 456, 788

Kurt, C.M., & Dufour, R.J. 1998, *Rev. Mex. Astr. Ap.* 7, 202

Landau, L.D., & Lifshitz, E.M. 1960, *Electrodynamics of Continuous Media* (New York: Pergamon) §62.

Laor, A., & Draine, B.T. 1993, *ApJ*, 402, 441

Li, D., Bancroft, G.M., Fleet, M.E., & Feng, X.H. 1995, *Phys. Chem. Minerals* 22, 115

Li, A., & Draine, B.T. 2001, *ApJ*, 554, 778

Li, A., & Draine, B.T. 2002, *ApJ*, 572, 232

Lillie, C.F., & Witt, A.N. 1976 *ApJ*, 208, 64

Marcelli, A., Davoli, I., Bianconi, A., Garcia, J., Gargano, A., et al. 1985, *J. de Physique* 46, 107

Margon, B., Bowyer, S., & Stone, R.P.S. 1973, *ApJ*, 185, L113

Martin, P.G. 1970, *MNRAS*, 149, 221

Mathis, J.S., Cohen, D., Finley, J.P., & Krautter, J. 1995, *ApJ*, 449, 320

Mathis, J.S., Rumpl, W., & Nordsieck, K.H. 1977, *ApJ*, 217, 425

McLaughlin, B.M., & Kirby, K.P. 1998, *J. Phys. B*, 31, 4991

Misselt, K.A., Clayton, G.C., & Gordon, K.D. 1999, *ApJ*, 515, 128

Morgan, D.H., Nandy, K., & Thompson, G.I. 1976. *MNRAS*, 177, 531

Murthy, J., & Henry, R.C. 1995. *ApJ*, 448, 848

Ninkov, Z., Walker, G.A.H., & Yang, S. 1986, *ApJ*, 321, 425

Overbeck, J.W. 1965, *ApJ*, 141, 864

Paerels, F., Brinkman, A.C., van der Meer, R.L.J., Kaastra, J.S., Kuulers, E., Boggende, A.J.F. den, Predehl, P., et al. 2001, *ApJ*, 546, 338

Predehl, P., & Schmitt, J.H.M.M. 1995, *A&A*, 293, 889 (PS95)

Sasseen, T.P., & Deharveng, J.-M. 1996. *ApJ*, 469, 691

Schiminovich, D., Friedman, P.G., Martin, C., & Morrissey, P.F. 2001. *ApJ*, 563, L161

Schulz, N.S., Cui, W., Canizares, C.R., Marshall, H.L., Lee, J.C., Miller, J.M., & Lewin, W.H.G. 2002, *ApJ*, 565, 1141

Sharp, T., Wu, Z., Seifert, F., Poe, B., Doerr, M., & Paris, E. 1996, *Phys. Chem. Minerals*, 23, 17

Shimada, H., Imamura, M., Matsubayashi, N., Saito, T., Tanaka, T., Hayakawa, T., & Kure, S. 2000, *Topics in Catalysis*, 10, 265

Smith, R.K., Edgar, R.J., & Shafer, R.A. 2002, *ApJ*, 581, 562

Stolte, W.C., Samson, J.A.R., Hemmers, O., Hansen, D., Whitfield, S.B., & Lindle, D.W. 1997, *J. Phys. B*, 30, 4489

Takei, Y., Fujimoto, R., Mitsuda, K., & Onaka, T. 2002, *ApJ*, 581, 307

Tanaka, Y., & Lewin, W.H.G. 1995, in *X-Ray Binaries*, ed. W.H.G. Lewin, J. van Paradijs, & E.P.J. van den Heuvel (Cambridge: Cambridge Univ. Press), 126

Ueda, Y., Asai, K., Yamaoka, K., Dotani, T., & Inoue, H. 2001, *ApJ*, 556, L87

van Aken, P.A., & Liebscher, B. 2002, *Phys. Chem. Minerals*, 29, 188

van Aken, P.A., Liebscher, B., & Styrsa, V.J. 1998, *Phys. Chem. Minerals*, 25, 323

van de Hulst, H.C. 1957, *Light Scattering by Small Particles* (New York: Wiley)

Verner, D.A. 1996, <http://www.pa.uky.edu/~verner/photo.html>

Verner, D.A., Ferland, G.J., Korista, K.T., & Yakovlev, D.G. 1996, *ApJ*, 464, 487

Verner, D.A., & Yakovlev, D.G. 1995, *A&A Suppl.*, 109, 125

Weingartner, J.C., & Draine, B.T. 2001, *ApJ*, 548, 296 (WD01)

Wiscombe, W.J. 1980, *Appl. Opt.*, 19, 1505

Wiscombe, W.J. 1996, NCAR Technical Note NCAR/TN-140+STR,
ftp://climate.gsfc.nasa.gov/pub/wiscombe/SingleScatt/Homogen_Sphere/Exact_Mie/NCARMieReport.pdf

Witt, A.N. 1977, *ApJS*, 35, 1

Witt, A.N., Friedmann, B.C., Sasseen, T.P. 1997. *ApJ*, 481, 809

Witt, A.N., Petersohn, J.K., Bohlin, R.C., O'Connell, R.W., Roberts, M.S., et al., 1992. *ApJ*, 395, L5

Woo, J.W. 1995, *ApJ*, 447, L129

Woo, J.W., Clark, G.C., Day, C.S.R., Nagase, F., & Takeshima, T. 1994, *ApJ*, 436, L5

Wu, Z., Seifert, F., Poe, B., & Sharp, T. 1996, *J. Phys: Condensed Matter*, 8, 3323.

Yao, Y., Zhang, S.N., Zhang, X.L., & Feng, Y.X. 2003, *astro-ph/0303149v1*